Chem. Rev. **2004,** *104,* 5717–5735

Muon-Spin Rotation Studies of Electronic Properties of Molecular Conductors and Superconductors

Stephen J. Blundell*

Department of Physics, Oxford University, Clarendon Laboratory, Parks Road, Oxford OX1 3PU, United Kingdom

Received March 16, 2004

Contents

1. Introduction

The muon is a versatile probe that can be used to study molecular conductors and superconductors. Both positive and negative muons can be produced in accelerators, but it is mainly the *positive* muon that is used for experiments on the solid state. The negative muon μ^-, which implants close to an atomic nucleus, is generally much less sensitive to the phenomena of interest (magnetism, superconductivity, etc.) than the site of the implanted positive muon μ^+, which sits well away from nuclei in regions of large electron density. In fact, even though the positively charged muon is a lepton and therefore essentially a heavy antielectron, for our purpose, it is more useful to consider it as a light proton.

The muon is found in nature as the dominant constituent of the cosmic rays arriving at sea level. Early experiments therefore used the freely available cosmic ray muons. For research work today, it is necessary to use the much more intense beams of muons available at synchrotron and cyclotron facilities. It is important to realize that, in contrast to neutron and X-ray techniques, scattering is *not* involved; muons are implanted into a sample of interest and reside there for the rest of their short lives, to never emerge again. It is the positrons (antielectrons) into which they decay that are released from the sample and yield information about the muons from which they came. It is quite incorrect therefore to refer to the technique as “muon scattering”, but *muon implantation* would be more correct. The abbreviation usually used is μSR, which stands for muon-spin rotation or sometimes muon-spin relaxation (for general reviews of the μSR technique, see refs 1−5). This abbreviation emphasizes that it is the spin precession or spin relaxation of the muon that is the crucial experimental observable. This makes the technique similar to nuclear magnetic resonance (NMR) and electron-spin resonance (ESR), although one important difference is that the muon beams can be produced with 100% polarization. For NMR and ESR, the polarization of the nuclear or electron spins is very far from 100%, so that a radio frequency or microwave photon is needed to resonantly perturb the system and obtain a signal. In μSR, no such photon is needed and the measurement is usually performed nonresonantly. Therefore, it is also incorrect to refer to the technique as “muon resonance” (although there are certain specialized applications of the technique that also employ radio frequency excitation[6]).

It turns out that μSR is extremely useful for studying various magnetic and superconducting systems. As will be described in more detail below, this is because the frequency of the spin precession of the implanted muon (as measured by the time dependence of the spatial asymmetry in the decay positron

Stephen Blundell is Professor of Physics at Oxford University. He received a B.A. in physics and theoretical physics in 1989 and a Ph.D. in 1993, both from the University of Cambridge. In 1993, he moved from the Cavendish Laboratory in Cambridge to the Clarendon Laboratory in Oxford, initially as a research fellow and from 1997 as a member of the faculty. He is a professorial fellow of Mansfield College, Oxford and the author of a textbook on magnetism, which was published in 2001. His research has focused on using muons to explore the magnetic and superconducting properties of various materials, including organic and molecular magnets and superconductors, magnetic oxides, and frustrated systems. He also has an active interest in using high-field magnetotransport to study Fermi surfaces of molecular metals and related systems.

---

* To whom correspondence should be addressed. Telephone: 44-1865-272-200. Fax: 44-1865-272-400. E-mail: s.blundell@physics.ox.ac.uk.

10.1021/cr030632e CCC: $48.50

Table 1. Properties of the Muon, Pion, Electron, and Proton

property	μ^+	π^+	e	p
mass	1.8835×10^{-28} kg	2.488×10^{-28} kg	9.1094×10^{-31} kg	1.6726×10^{-27} kg
	105.66 MeV	139.57 MeV	0.511 00 MeV	938.27 MeV
	$0.1126m_p$	$0.1487m_p$	$m_p/1836.2$	m_p
	$206.768m_e$	$273.13m_e$	m_e	$1836.2m_e$
charge	$+e$	$+e$	$-e$	$+e$
spin	$^1/_2$	0	$^1/_2$	$^1/_2$
magnetic moment	4.4904×10^{-26} J T^{-1}	0	-928.48×10^{-26} J T^{-1}	1.4106×10^{-26} J T^{-1}
	$3.1833\mu_p$	0	$-658.21\mu_p$	μ_p
	$8.891\mu_N$	0	$-1838.3\mu_N$	$2.7928\mu_N$
	$4.842 \times 10^{-3}\mu_B$	0	$-1.001\mu_B$	$1.521 \times 10^{-3}\mu_B$
gyromagnetic ratio/(2π)	135.53 MHz T^{-1}	0	28 024.21 MHz T^{-1}	42.577 MHz T^{-1}
lifetime	$2.197\,03 \times 10^{-6}$ s	0.0260×10^{-6} s	$>4 \times 10^{23}$ years	$>2 \times 10^{26}$ years[22]

emission) is directly related to the magnetic field at the muon site; hence, the muon can be used as a "microscopic magnetometer". Muons have been found to be effective probes of various types of condensed matter physics phenomena and their use has been aided by the development of a number of accelerator facilities, most notably TRIUMF (Vancouver, Canada),[7] PSI (PSI = Paul Scherrer Institute, Villigen, near Zürich, Switzerland),[8] ISIS (RAL = Rutherford Appleton Laboratory, Oxfordshire, U.K.),[9,10,11] RIKEN-RAL (also at RAL),[12,13] KEK (Tsukuba),[14,15] and Dubna, Russia. The technique requires the use of bulk samples because, in the case of the most often used "surface muons" (muons produced from the stopped pions in the surface of a target), the muons are formed with energy 4 MeV and penetrate a few hundred micrometers into any sample.

Muons turn out to be a very natural probe of magnetism (for examples, see refs 4 and 16−21), but the purpose of this article is to show how muons can also be used to study various types of molecular conductors. In the following two sections, I will review the basic physics of the muon and muonium (μ^+e^-). Subsequent sections will describe applications of the technique to organic donors, organic metals, organic superconductors, and conducting polymers.

2. The Muon

Some properties of the muon, pion, electron, and proton are tabulated in Table 1. The mass of the muon is intermediate between that of the electron and the proton and thus so are its magnetic moment and gyromagnetic ratio. The latter is the constant of proportionality between angular momentum and magnetic moment. Cosmic rays provide a major source of muons (roughly 1 muon arrives vertically on each square centimeter of the earth's surface every minute) but to obtain the necessary intensity (to perform an experiment in a reasonable amount of time), it is necessary to obtain muons from accelerator sources. High energy proton (p) beams (produced using synchrotrons or cyclotrons) are fired into a target (usually graphite) to produce pions (π^+) via the reaction

$$p + p \rightarrow \pi^+ + p + n \tag{1}$$

and the pions subsequently decay into muons (μ^+)

$$\pi^+ \rightarrow \mu^+ + \nu_\mu \tag{2}$$

where ν_μ is a muon−neutrino. The pion decay is a two-body decay and is therefore particularly simple. For example, consider the pions that are produced at rest in the laboratory frame. To conserve momentum, the muon and the neutrino must have equal and opposite momentum. The pion has zero spin (see Table 1); therefore, the muon spin must be opposite to the neutrino spin. One useful property of the neutrino is that its spin is aligned antiparallel with its momentum (it has negative helicity), and this implies that the muon spin is similarly aligned (see Figure 1). Thus, by selecting pions that stop in the target (and that are therefore at rest when they decay), one has a means of producing a beam of 100% spin-polarized muons. This is the method most commonly used for producing muon beams for condensed matter physics research, although other configurations are in use. The polarized muons are transported to the sample through a combination of dipole-steering magnets and quadrupole-focusing magnets. Filters consisting of a combination of electric and magnetic fields are used for a momentum/mass selection of the particles to eliminate contaminating positrons (antielectrons) in the beam. These positrons arise from muons that decay before reaching the sample.

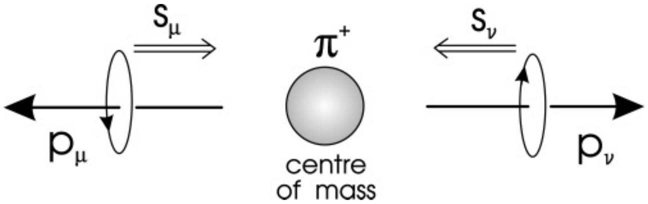

Figure 1. Decay of the pion. The muon neutrino ν_μ (right-hand side) has a negative helicity in the pion rest frame. Because of conservation of angular momentum, the muon will also have its spin S_μ antiparallel to its momentum.

Muons are implanted into the sample with an energy that is at least 4 MeV. They lose energy very quickly (in 0.1−1 ns) to a few keV by ionization of atoms and scattering with electrons. Then, the muon begins to undergo a series of successive electron capture and loss reactions, which reduce its energy to a few hundred electronvolts in about a picosecond. If muonium (μ^+e^-, see section 3) is ultimately formed, then electron capture wins and the last few electronvolts are shed by inelastic collisions between the muonium atom and the host atoms. All of these effects are very fast, so that the muon (or muonium) is thermalized very rapidly (rapid in comparison with the time scales of muon decay, see below). Moreover, the effects are all Coulombic in origin and do not interact with the muon spin, so that the muon is

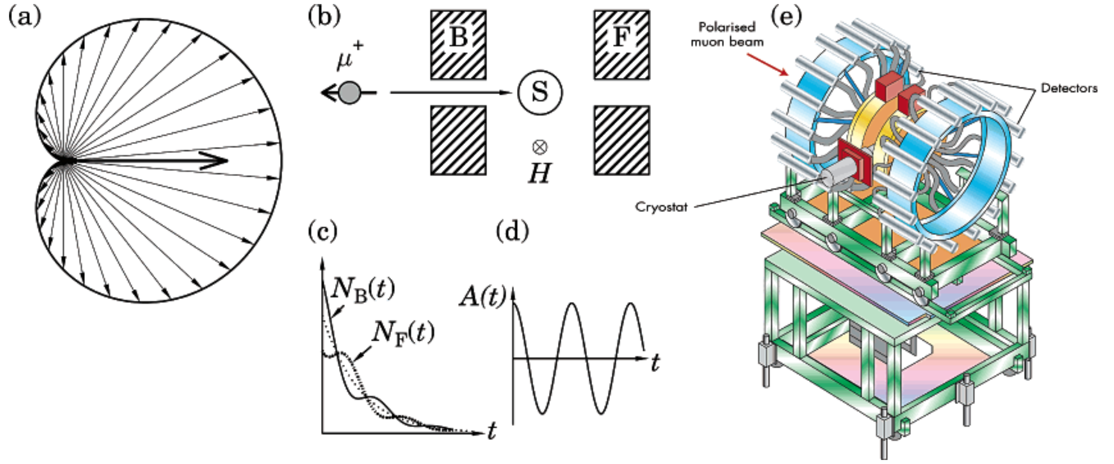

Figure 2. (a) Angular distribution of emitted positrons with respect to the initial muon-spin direction. The expected distribution for the most energetically emitted positrons is shown. (b) Schematic illustration of a μSR experiment. A spin-polarized beam of muons is implanted in a sample S. After decay, positrons are detected in either a forward detector F or a backward detector B. If a transverse magnetic field H is applied to the sample as shown, then the muons will precess. (c) Number of positrons detected in the forward (- - -) and backward (—) detectors. The dotted line shows the average of the two signals. (d) Asymmetry function. (e) Spectrometer on the MuSR beamline at ISIS, the Rutherford Appleton Laboratory, Oxfordshire, U.K. (courtesy of ISIS Pulsed Muon Facility).

thermalized in matter without appreciable depolarization. This is a crucial feature for muon-spin rotation experiments. One may be concerned that the muon may only measure a region of sample that has been subjected to radiation damage by the energetic incoming muon. This does not appear to be a problem because there is a threshold energy for vacancy production, which means that only the initial part of the muon path suffers much damage. Beyond this point of damage, the muon still has sufficient energy to propagate through the sample a further distance, thought to be about 1 μm, leaving it well away from any induced vacancies.[23]

Thus, the muons are stopped in the specimen of interest and decay after a time t with a probability proportional to e^{-t/τ_μ}, where $\tau_\mu = 2.2\ \mu$s is the lifetime of the muon. The muon decay is a three body process

$$\mu^+ \rightarrow e^+ + \nu_e + \bar{\nu}_\mu \tag{3}$$

and so the energy of the positron e^+ (which is the only particle produced in this reaction that we have a sensible hope of reliably detecting) may vary depending on how momentum is distributed between the three particles (subject to the constraint that the total vector momentum will sum to zero, the initial momentum of the stopped muon). The decay involves the weak interaction and thus has the unusual feature of not conserving parity.[24] This phenomenon (which also lies behind the negative helicity of the neutrino) leads to a propensity for the emitted positron to emerge predominantly along the direction of the muon spin when it decayed. The decay probability of the muon can be calculated from the electroweak theory, which involves parity violating interactions. The probability per unit time for positron emission at an angle θ to the muon spin is given by

$$dW(\epsilon,\theta) = d\epsilon\ d\cos\theta\ \frac{n(\epsilon)}{\tau_\mu}\{1 + a(\epsilon)\cos(\theta)\}. \tag{4}$$

Here, ϵ is the normalized positron energy $E/E_{\max}$, $a(\epsilon) = (2\epsilon - 1)/(3 - 2\epsilon)$ is the asymmetry factor, and $n(\epsilon) = \epsilon^2(3 - 2\epsilon)$.

The angular distribution of emitted positrons is shown in Figure 2a for the case of the most energetically emitted positrons. In fact, positrons over a range of energies are emitted, so that the net effect is something not quite as pronounced, but one can nevertheless follow the polarization of an ensemble of precessing muons with arbitrary accuracy, providing that one is willing to take data for long enough.

A schematic diagram of the experiment is shown in Figure 2b. A muon, with its polarization aligned antiparallel to its momentum, is implanted in a sample. It is antiparallel because of the way that it was formed (see above); therefore, the muon enters the sample with its spin pointing along the direction from which it came. If the muon is unlucky enough to decay immediately, then it will not have time to precess and a positron will be emitted preferentially into the backward detector. If the muon lives a little longer, it will have time to precess; therefore, for example, if it lives for half a revolution, the resultant positron will be preferentially emitted into the forward detector. Thus, the positron beam from an ensemble of precessing muons can be likened to the beam of light from a lighthouse.

The time evolution of the number of positrons detected in the forward and backward detector is described by the functions $N_F(t)$ and $N_B(t)$, respectively, and these are shown in Figure 2c. Because the muon decay is a radioactive process, these two terms sum to an exponential decay. Thus, the time evolution of the muon polarization can be obtained by examining the normalized difference of these two functions via the asymmetry function $A(t)$, given by

$$A(t) = \frac{N_B(t) - N_F(t)}{N_B(t) + N_F(t)}, \tag{5}$$

and is shown in Figure 2d.

This experimentally obtained asymmetry function has a calculable maximum value, $A_{\max}$, for a particular experimental configuration, which depends on the initial beam polarization (usually very close to 1), the intrinsic asymmetry of the weak decay, the efficiency of the detectors for positrons of different energies, and the solid angle subtended by the detectors, and usually turns out to be around $A_{\max} \sim 0.25$. The function can be normalized to 1, in which case it expresses the spin autocorrelation function of the muon, $G(t) = A(t)/A_{\max}$, which represents the time-dependent spin polarization of the ensemble of muons.

Figure 2e shows a drawing of a muon spectrometer used at the ISIS pulsed muon facility. Two banks of detectors are arranged on either side of the sample and the grouped signals from each bank constitute the forward and backward detectors of Figure 2b. Each detector consists of a piece of scintillator light guide connected to a photomultiplier tube. The spectrometer is equipped with a variety of possible sample environments, including a furnace, dilution refrigerator, He^4 cryostat, and closed cycle refrigerator, with magnetic fields up to 0.2 T in the transverse or longitudinal directions.

3. Muonium

Depending on its chemical environment, the muon can thermalize and pick up an electron and form a neutral atomic state called muonium (abbreviated Mu = μ^+e^-), which is an isotope of atomic hydrogen. Muonium (Mu = μ^+e^-) has a Bohr radius and Bohr energy close to the value for hydrogen (see Table 2).

Table 2. Properties of Atomic Muonium and Atomic Hydrogen (Protium)

property	muonium = μ^+e^-	hydrogen = p^+e^-
mass	$0.1131m_H$	m_H
	$207.77m_e$	$1837.2m_e$
reduced mass	$0.9956\mu_H$	μ_H
Bohr radius	$1.0044a_0$	$a_0 = 0.5292$ Å
ionization energy	$0.9956R_\infty$	$R_\infty = 13.6058$ eV
hyperfine-coupling constant	$3.1423A_H$	A_H
	$2\pi \times 4463.3$ MHz	$2\pi \times 1420.4$ MHz

In muonium, the electronic spin and the muon spin are coupled by a hyperfine interaction, which I will initially assume is isotropic. This leads to two energy levels, a lower singlet state and a higher triplet state. In a magnetic field, the triplet levels split and the energy levels move as shown in the Breit−Rabi diagram in Figure 3.

This can be treated mathematically as follows: we consider a free, isotropic muonium state and write the Hamiltonian for a magnetic field B parallel to the z axis as

$$H/\hbar = -\gamma_\mu \boldsymbol{I}\cdot\boldsymbol{B} + \gamma_e \boldsymbol{S}\cdot\boldsymbol{B} + A\boldsymbol{S}\cdot\boldsymbol{I} = -\gamma_\mu I_z B + \gamma_e S_z B + A\boldsymbol{S}\cdot\boldsymbol{I} \quad (6)$$

where $\boldsymbol{I}$ and $\boldsymbol{S}$ are the muon- and electron-spin operators and A is the (isotropic) hyperfine-coupling constant (expressed as an angular frequency, so that $\hbar A$ has the units of energy). In this equation, all terms are in angular frequency units. The eigenvalues and eigenvectors of this Hamiltonian can be calculated, and the results are shown in Table 3. On the basis of the spin Hilbert space, one can use the product of the muon and electron spin up and down vectors, $|\Psi\rangle = |\chi_\mu\rangle \otimes |\chi_e\rangle = |\chi_\mu\chi_e\rangle$.

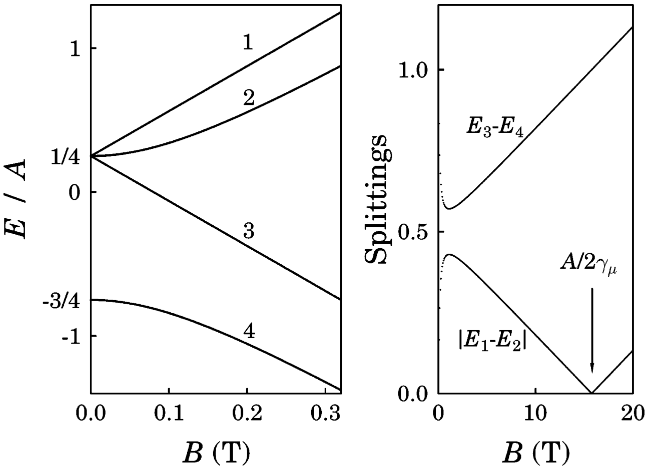

Figure 3. Breit−Rabi diagram for isotropic muonium with a hyperfine constant appropriate for free (vacuum) muonium. Also shown are the splittings between pairs of levels over a larger range of the magnetic field. Levels 1 and 2 cross at a field of $2mB_0/(1 - m^2) \sim A/2\gamma_\mu = 16.5$ T for free muonium.

Table 3. Eigenstates and Eigenvalues of Muonium[a]

eigenvector	eigenvalue
$\lvert\Psi_1\rangle = \lvert\uparrow_\mu\uparrow_e\rangle$	$E_1/\hbar = [A/4]\,(1 + 2mB/B_0)$
$\lvert\Psi_2\rangle = \alpha\lvert\uparrow_\mu\downarrow_e\rangle + \beta\lvert\downarrow_\mu\uparrow_e\rangle$	$E_2/\hbar = -[A/4]\,(1 - 2\sqrt{1 + (B/B_0)^2})$
$\lvert\Psi_3\rangle = \lvert\downarrow_\mu\downarrow_e\rangle$	$E_3/\hbar = [A/4]\,(1 - 2mB/B_0)$
$\lvert\Psi_4\rangle = \beta\lvert\uparrow_\mu\downarrow_e\rangle - \alpha\lvert\downarrow_\mu\uparrow_e\rangle$	$E_4/\hbar = -[A/4]\,(1 + 2\sqrt{1 + (B/B_0)^2})$
$B_0 = A/\{\gamma_\mu + \gamma_e\}$, $m = (\gamma_e - \gamma_\mu)/(\gamma_e + \gamma_\mu) \approx 0.9904$	

$$\alpha = [1/\sqrt{2}]\,\sqrt{1 - [(B/B_0)/\sqrt{1 + (B/B_0)^2}]},$$

$$\beta = [1/\sqrt{2}]\,\sqrt{1 + [(B/B_0)/\sqrt{1 + (B/B_0)^2}]}$$

[a] For free muonium, $B_0 = 0.1585$ T.

As can be seen from Figure 3, the eigenstates at low fields are one triplet state and one singlet state. The eigenstates in this regime are given by the basis vectors of the $|F = S + I, m_F\rangle$ basis. At high fields (the Paschen-Back regime), the eigenstates are given by the basis vectors of the $|m_S, m_I\rangle$ basis, where m_i (i = F, S, and I) is the eigenvalue of the z component of F, S, and I. In this regime ($\gamma_e B \gg A$), the electron and muon spins are decoupled.

Suppose one implants muons in a sample and applies a magnetic field in the direction of the spin polarization. It then can be shown that the muon spin polarization

$$P_z(t) = \frac{1 + 2(B/B_0)^2}{2\{1 + (B/B_0)^2\}} + \frac{1}{2\{1 + (B/B_0)^2\}}\cos(\omega_{24}t) \quad (7)$$

where $\omega_{24} = A\sqrt{1 + (B/B_0)^2}$ and, for free muonium, B_0 = 0.1585 T. The incoming muons are spin polarized, while the electrons that are picked up to form the muonium are not usually spin-polarized (unless the sample is ferromagnetic). Therefore, the initial states will be a combination of $|\uparrow_\mu\uparrow_e\rangle$ and $|\uparrow_\mu\downarrow_e\rangle$ (see Table 3).

In all cases, the muonium can be studied by measuring precession signals in an applied magnetic field or by using a technique known as repolarization (Figure 4). In this latter method, a longitudinal magnetic field is applied to the sample, along the initial muon-spin direction, and as the strength of the magnetic field increases, the muon and electron spins are progressively decoupled from the hyperfine field. For isotropic muonium, half of the initial polarization of implanted muons is lost because of the hyperfine coupling, but this is recovered in a sufficiently large applied field (Figure 4), allowing an estimate of the strength of the hyperfine field. This occurs because, on increasing the magnetic field B, the Zeeman energy dominates and the electron and muon spins become decoupled (i.e., $\alpha \rightarrow 0$ and $\beta \rightarrow 1$ in Table 3). This "repolarization" is illustrated in Figure 4 and given by

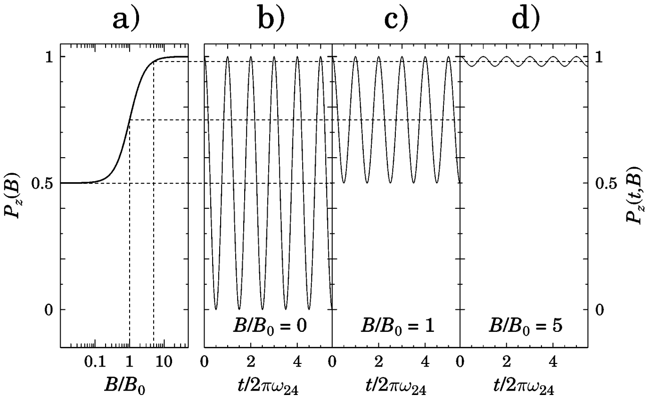

Figure 4. Effect of "repolarization" of the initial muon polarization, shown in a, is the result of the oscillations plotted in b−d being averaged out when the hyperfine frequency ω_{24} is too fast to be observed. The plots in b−d are produced from eq 7, while that in a is from eq 8.

$$P_z(B) = \frac{1 + 2(B/B_0)^2}{2\{1 + (B/B_0)^2\}}, \tag{8}$$

(see eq 7). For anisotropic muonium, the repolarization is slightly more complicated (for example, see ref 25).

In metallic samples, the positive charge of the muon is screened by conduction electrons, which form a cloud around the muon, of a size given by a Thomas−Fermi screening length. Thus, μ^+, rather than muonium, is the appropriate particle to consider in a metal. (The endohedral muonium found in alkali fulleride superconductors is the only known example of a muonium state in a metal.) In insulators and semiconductors, screening cannot take place; therefore, the muon is often observed in these systems either as muonium or is found to be chemically bound to one of the constituents, particularly to oxygen if it is present. Isotropic muonium states are found in many semiconducting and insulating systems. The value of the hyperfine-coupling strength is close to that for vacuum (free) muonium if the band gap is large (see Figure 5). For materials with smaller band gaps, the hyperfine coupling is lower, reflecting the greater delocalization of the electron spin density on to neighboring atoms.[1] This occurs because the greater the disparity between the levels of the states to be mixed, the smaller is the degree of mixing (i.e., the more the muonium retains its atomic character).[27]

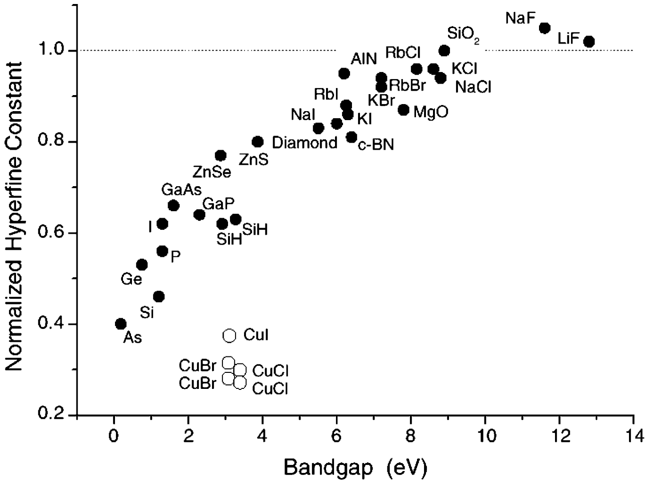

Figure 5. Hyperfine constants for isotropic muonium centers in semiconductors and dielectrics, relative to the vacuum-state value of 4463.3 MHz (reprinted with permission from ref 26, copyright 2003 IOP Publishing Limited).

In Si, a substantial fraction of neutral muonium is also found in a most unexpected place, wedged into the center of a stretched Si−Si bond or "bond-center" (see ref 28 for a review of muonium states in semiconductors). This state is extremely immobile and surprisingly turns out to be the thermodynamically more stable site. Its hyperfine coupling is much lower than that of the tetrahedral state, typically less than 10% of the vacuum value. Furthermore, the coupling is very anisotropic, with axial symmetry about the ⟨111⟩ crystal axis (i.e., along the Si−Si bonds), so that the energy levels behave in a different manner to that indicated in Figure 3. These states have rather interesting dynamics and can undergo charge- and spin-exchange processes, cycling rapidly between positive and negative charge states via interaction with conduction electrons.[29] The characterization of all of these states is important because it is found that atomic hydrogen is present in most semiconductors and is able to passivate (i.e., deactivate) the dangling bonds in amorphous silicon, allowing it to show semiconducting properties. Hydrogen is inevitably present in all semiconductors, often becoming incorporated during material production from hydride gases or during etching, but the low concentration makes direct spectroscopic studies very difficult. Using muonium as an analogue for hydrogen has therefore been a promising method of obtaining a great deal of spectroscopic information concerning this problem.[1,26,30]

In semimetals, the electron density is low and the screening of the muon charge is far from perfect. This is thought to be responsible for the large muon Knight shift in antimony (~1%).[1,31,32] In graphite, the positive muon also retains its full polarization, but a molecular radical state can also exist; transitions in and out of such a localized paramagnetic state can enhance the muon Knight shift and the muon relaxation rate.[33,34]

An interesting situation occurs in the case of C_{60} in which muonium can implant inside the buckyball cage (this state is called endohedral muonium). The unpaired electron part of the muonium greatly enhances the sensitivity to scattering from conduction electrons; therefore, this state is extremely useful for studying alkali-fulleride superconductors.[35] It is also possible to form a muonium radical by external addition, essentially muonium attacking the outside of a buckyball, breaking a double bond, and ending up covalently bonded to a single-saturated carbon atom. This center is very sensitive to the molecular dynamics of the local environment and has been used to extract the correlation time for molecular reorientation.[36]

Muonium states can also be formed in many organic systems and allow a unique form of radical spectroscopy.[37] Muonium adds to unsaturated bonds to form muonated free radicals. Addition of muonium at the carbon−carbon double bond in ethene (see Figure 6a) produces the muoniated ethyl radical. The radical is electrically neutral but has an electronic doublet ground state because of the unpaired electron remaining on the unlabeled carbon atom. As described below, it is the hyperfine coupling between the muon and the unpaired electron that can be the source of information on the molecular dynamics (showing, for example, that $-CH_2Mu$ reorients less readily than $-CH_3$). As another example, addition to benzene (C_6H_6) leads to the muonated cyclohexadienyl radical (C_6H_6Mu), as shown in Figure 6b. The advantage of the muon technique is that one can work with concentrations down to just one muonated radical at a time in an entire macroscopic sample. In contrast, ESR detection needs $\sim 10^{12}$ radicals in a cavity, forbidding measurements at high temperatures where the radicals become mobile and terminate by combination. The technique has been applied to radicals in various environments,[37] including those absorbed on surfaces[38] and also to liquid crystals.[39]

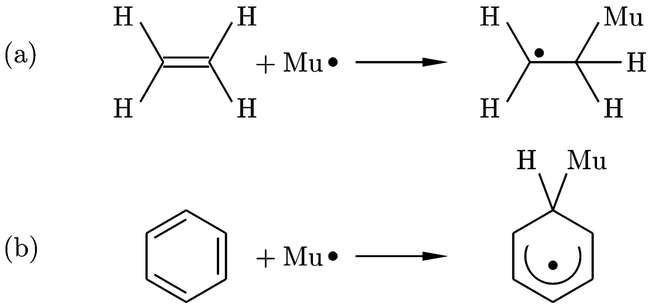

Figure 6. Muonium addition to (a) ethene and (b) benzene.

In muoniated radicals, a weakened hyperfine interaction persists between the electron and muon spins and also between the electron and any other nearby nuclei with magnetic moments. There are two contributions to the hyperfine interaction of any muon (or nucleus) in an organic radical: the Fermi contact interaction of any unpaired electron spin, which is independent of the orientation of the radical in a magnetic field, and the dipolar magnetic interaction of the pointlike muon (or nucleus) and the unpaired electron spin (which is distributed in space). The latter interaction reflects the distribution of the electron spin and is anisotropic. The hyperfine-interaction tensor is the sum of an isotropic part A_μ^{iso} and a traceless dipolar part D_μ. In the case of axial symmetry, the latter can be described by a single parameter $D_\mu^{\|}$, the largest principal value. The other two principal values are $D_\mu^{\perp} = -D_\mu^{\|}/2$.[25] Fluctuations in the isotropic or anisotropic components of the hyperfine interaction because of inter- or intramolecular motion strongly affect the spin−lattice relaxation, and longitudinal μSR measurements can therefore be used to extract dynamical information.[40,41]

At very high fields, when the electron and muon spins are completely decoupled, the initial muon polarization is preserved. However, at certain values of the magnetic field, a level crossing of energy levels may occur. In fact, there is one occurring at a very high field in free muonium (see Figure 3b). Interactions between the muon−electron system and nuclei in the host material cause the pure Zeeman states to mix near these level crossings, thereby avoiding the crossing, and this can lead to a loss of polarization, the measurement of which gives rise to the technique of avoided level-crossing (ALC) spectroscopy.[42−45] ALC transitions can be classified into types based on ΔM, the difference in the total magnetic quantum number between the original states involved.[42,43] In Δ_1 transitions, where $\Delta M = 1$, the states differ only in the muon spin; the resonant state involves an oscillation of the muon-spin component in the direction of the longitudinal field and takes place around a magnetic field value given by

$$B_0^{\Delta_1} = \left|\frac{A_\mu}{2\gamma_\mu}\right|, \tag{9}$$

where A_μ is the muon-hyperfine constant. This level crossing is avoided by coupling of the two Zeeman states through the dipolar part of the hyperfine interaction.[43] In a polycrystalline sample, D_μ, the anisotropy in the hyperfine coupling, will give rise to an asymmetric ALC line shape.[37] The mean muon-spin precession frequency "on resonance" in high fields is $\omega = D_\mu^{\perp}/2$. With decreasing axial anisotropy, the resonance narrows and loses intensity as it becomes smaller than the inverse muon lifetime $1/\tau_\mu = 0.45$ MHz.[46]

For Δ_0 transitions, where $\Delta M = 0$, the resonant state involves an exchange between the muon spin and a nuclear spin, usually a proton. The resonance is therefore essentially a muon−nucleus-spin flip flop. The crossing of the levels is avoided by indirect coupling of both Zeeman states to a third one. This ALC occurs at a magnetic field[42]

$$B_0^{\Delta_0}(M) = \left|\frac{A_\mu - A_k}{2(\gamma_\mu - \gamma_k)} - \frac{(A_\mu)^2 - 2M(A_k)^2}{2\gamma_e(A_\mu - A_k)}\right| \tag{10}$$

where $I^k \geq M \geq (-I^k + 1)$ and I^k is the spin of the nucleus. If the nucleus is a proton, i.e., $I^k = 1/2$, the equation simplifies to

$$B_0^{\Delta_0} = \left| \frac{A_\mu - A_p}{2(\gamma_\mu - \gamma_p)} - \frac{A_\mu + A_p}{2\gamma_e} \right| \tag{11}$$

where A_p is the proton-hyperfine constant and γ_p and γ_e are the proton and electron gyromagnetic ratios, respectively. Because all of our measurements are on solid polycrystalline samples, for the Δ_1 transitions, there is a characteristic asymmetric broadening of the line shape because of D_μ, the anisotropic dipolar part of the hyperfine-interaction tensor. Loss of polarization from the coupled spin system by relaxation effects leads to additional symmetrical broadening in both types of resonance. Often one finds that some weak resonances that are only visible at higher temperatures can be well-fitted by Lorentzians, whereas Δ_1 resonances that are also visible at low temperatures need a more sophisticated treatment to match their asymmetric line shapes. Polycrystalline averaging of the numerical solution of the Wangsness–Bloch dynamical equations[47–49] for a muon–electron-coupled state with axially symmetric hyperfine tensor can be used in the fitting, allowing dipolar broadening and electronic spin relaxation rate parameters to be estimated.

There is also a transition with $\Delta M = 2$, a muon–nuclear-spin flip-flip transition, but it is usually very weak and narrow.

As described earlier, muonium in muoniated radicals is often regarded as a light isotope of hydrogen. To make a meaningful comparison of proton-hyperfine interactions A_p (where I have taken $k = p$) and muon-hyperfine interactions A_μ, the latter is often multiplied by the ratio of the magnetic moments of the muon and the proton, i.e.

$$A'_\mu = \frac{\mu_p}{\mu_\mu} A_\mu = 0.3141 A_\mu \tag{12}$$

It is then possible to compare these values to those obtained for A_p (e.g., from ESR experiments). They will usually not be identical, because the different masses of hydrogen and muonium will have an influence on the bonding lengths and bonding angles and therefore also on the contact interaction (the isotope effect). Usually $A'_\mu/A_p \approx 1.3$, but higher values have been observed [e.g., $A'_\mu/A_p \approx 1.74$ for ethene ($H_2C{=}CH_2$)].[50]

The implanted muonium states can be described as diamagnetic or paramagnetic, depending on whether they experience a hyperfine coupling to unpaired electron-spin density. The most commonly encountered diamagnetic species is μ^+, the free muon, but negatively charged muonium ($Mu^- = \mu^+e^-e^-$) is also diamagnetic in this sense. (Note that positively charged muonium Mu^+ is identical with μ^+.) Another diamagnetic species is formed from the analogue of protonation reactions (in which a muon sticks to the lone pair on an oxygen or nitrogen atom) as in

$$H_2O + \mu^+ \rightarrow H_2OMu^+ \tag{13}$$

or

$$N_2 + \mu^+ \rightarrow N_2Mu^+ \tag{14}$$

In these reactions, the symbol Mu^+ is used to emphasize the fact that the muon has thermalized. A further uncharged diamagnetic species may be obtained if the charged species H_2OMu^+ reacts with another water molecule, leaving muonium substituted in a neutral molecule[51]

$$H_2O + H_2OMu^+ \rightarrow HMuO + H_3O^+ \tag{15}$$

Neutral muonium, $Mu = \mu^+e^-$, is a paramagnetic species. In section 7, the interesting case of a muon attached to a conducting polymer will be presented. The state of this muon is alternately diamagnetic and paramagnetic because of an intermittent hyperfine coupling between the muon and the diffusing radical electron. In all of these cases, an understanding of the location and nature of the muon site is extremely important, and a variety of theoretical techniques can be used to shed light on this[52] and their results, compared with the experimental values.

4. Muonium in Organic Donors

Many organic charge-transfer salts[53] are formed by combining electronic donors with electronic acceptors. The molecule tetracyanoquinodimethanide (TCNQ, see Figure 8) is an electronic acceptor, which is found in a number of interesting compounds. Often used donors include the molecule tetrathiafulvalene (TTF, see Figure 8) and its derivatives, such as bis(ethyl-

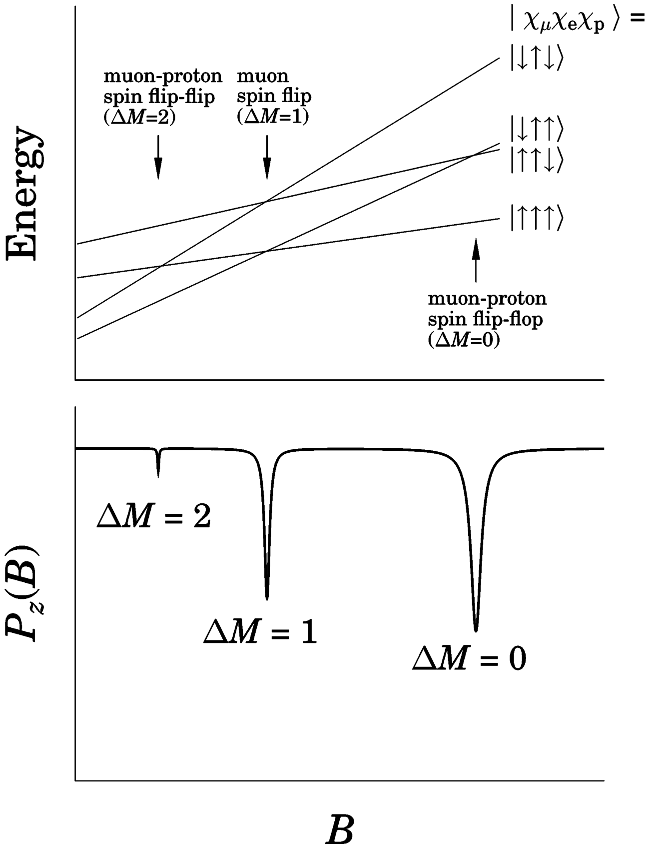

Figure 7. Upper panel: high-field energy diagram for a three-spin system. Lower panel: ALC resonances occur when states with opposite muon spin become near-degenerate in energy, after ref 37.

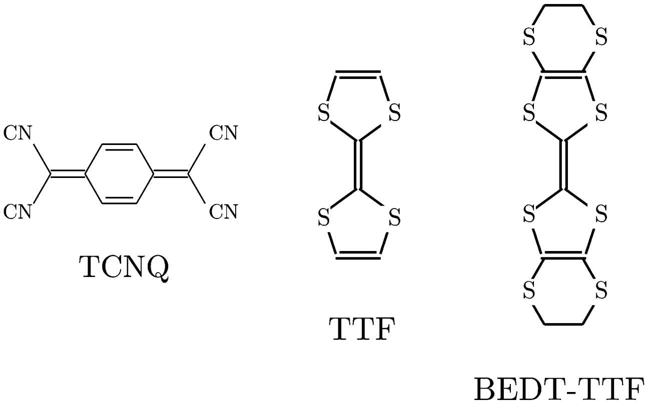

Figure 8. Molecules TCNQ, TTF, and BEDT-TTF.

enedithio)tetrathiafulvalene (BEDT-TTF), bis(ethylenedithio)tetraselenafulvalene (BETS), and TMTSF. These latter donors are well-known for forming the basis for many organic metals. In particular, BEDT-TTF (see Figure 8) turns out to be a very versatile donor, and a number of charge-transfer salts derived from BEDT-TTF have been found to be very good organic metals and sometimes superconductors. The BEDT-TTF molecules contain sulfur atoms on the side, and intermolecular S−S overlaps are the most important intermolecular interactions in these salts. BEDT-TTF salts are naturally layered, with alternating layers of the BEDT-TTF molecules, stacked side−side, so that the molecular orbitals overlap, and layers of anions. In this way, the charge-transfer salts are "organic−inorganic molecular composites" or "chemically constructed multilayers".[54] Within the BEDT-TTF layers, the molecules are in close proximity to each other, allowing substantial overlap of the molecular orbitals. Usually 2 (or sometimes 3) BEDT-TTF molecules will jointly donate an electron to the anion, and the charge transfer leaves behind a hole on the BEDT-TTF molecules. This means that the bands formed by the overlap of the BEDT-TTF molecular orbitals will be partially filled, leading to the possibility of metallic behavior. The transfer integrals, which parametrize the ease of hopping of electrons between BEDT-TTF molecules, will be relatively large within the BEDT-TTF planes. Conversely, in the direction perpendicular to the BEDT-TTF planes, the BEDT-TTF molecules are well-separated from each other; the transfer integrals will be much smaller in this direction. This results in electronic properties that for many purposes can be considered to be two-dimensional.[55,56] In the Mott insulator regime of these metals, the π system can be regarded as having a localized $S = {}^1/_2$ on each BEDT-TTF molecule.

The conducting or semiconducting charge-transfer salts have partly filled bands that are well-described by tight-binding bandstructures based on the overlapping molecular orbitals. In this situation, an electron donated to a molecule, e.g., following muonium addition, can become a delocalized band electron leaving the muon bonded to the molecule but in a diamagnetic environment. Crystals of the raw donor or acceptor molecules on the other hand are insulators, because there is no charge transfer. This means that, when muonium reacts with one of the molecules, the muonium electron remains localized on the molecule forming a muonium-radical species, which can be studied by the methods of muonium-radical spectroscopy, the results of which[57] will now be reviewed.

The electron donor TTF contains one central and two outer carbon double bonds, which might be expected to form radical states on muonium addition to a carbon atom. High transverse field (TF) muon-spin-rotation spectroscopy[58] can also be used to study the paramagnetic muon states because a pair of muon-spin-rotation signals are observed for each radical with frequencies given by

$$\omega_{1,2} = |\gamma_\mu B \pm A/2| \tag{16}$$

which are the high-field limits of $(E_3 - E_4)/\hbar$ and $(E_2 - E_1)/\hbar$ given in Table 3. Because the pair of frequencies is entirely defined by the applied field B and the isotropic hyperfine constant A, it is useful to use a frequency pair correlation function $C(A)$ to extract radical signals from a frequency spectrum $p(\omega)$, which is given by

$$C(A) = p(\omega_1(A, B))\, p(\omega_2(A, B)) \tag{17}$$

The TF measurements[57] measured on TTF using the PSI GPS instrument are shown in Figure 9. The striking beat structure seen in the muon-spin-rotation signal indicates the presence of signals close to the diamagnetic frequency $\gamma_\mu B$. In Figure 10, the frequency spectrum and hyperfine-correlation spectrum clearly shows a state with a very low hyperfine coupling in the region of 5 MHz. The fit to the time-dependent asymmetry in Figure 9 includes terms from a strongly coupled ($A \sim 300$ MHz) radical and a weakly coupled ($A \sim 5$ MHz) radical, and the sum of these signals plus the diamagnetic fraction accounts for almost all of the expected asymmetry.[57] ALC data[57] show a Δ_1 resonance at ~1.2 T, which can be associated with the strongly coupled radical. The high-coupling-constant radical is most likely to be associated with the outer C=C bond in TTF, which would lead to less molecular distortion than the inner C=C bond.[59] The central adduct may be responsible for the weakly coupled radical or possibly the addition to sulfur.[59]

For TCNQ, ALC spectra are shown in Figure 11. These data were taken in time-differential mode; therefore, the background here is very flat compared to similar data taken in time-integral mode. As found for TTF, the spectra are dominated by a single Δ_1 resonance, but it occurs here at a rather lower field, indicating a much smaller isotropic hyperfine coupling. The resonance is centered around 0.3 T at low temperature, with a very weak additional resonance appearing around 0.22 T at higher temperatures. The 0.3 T resonance accounts for almost all of the asymmetry, indicating that a single dominant radical state is very efficiently formed with a contact hyperfine coupling $A \sim 85$ MHz and a dipolar anisotropy $D \sim 10$ MHz.[57] This main resonance is probably due to muon addition to the nitrogen atoms, and calculations of the hyperfine coupling for this site agree well

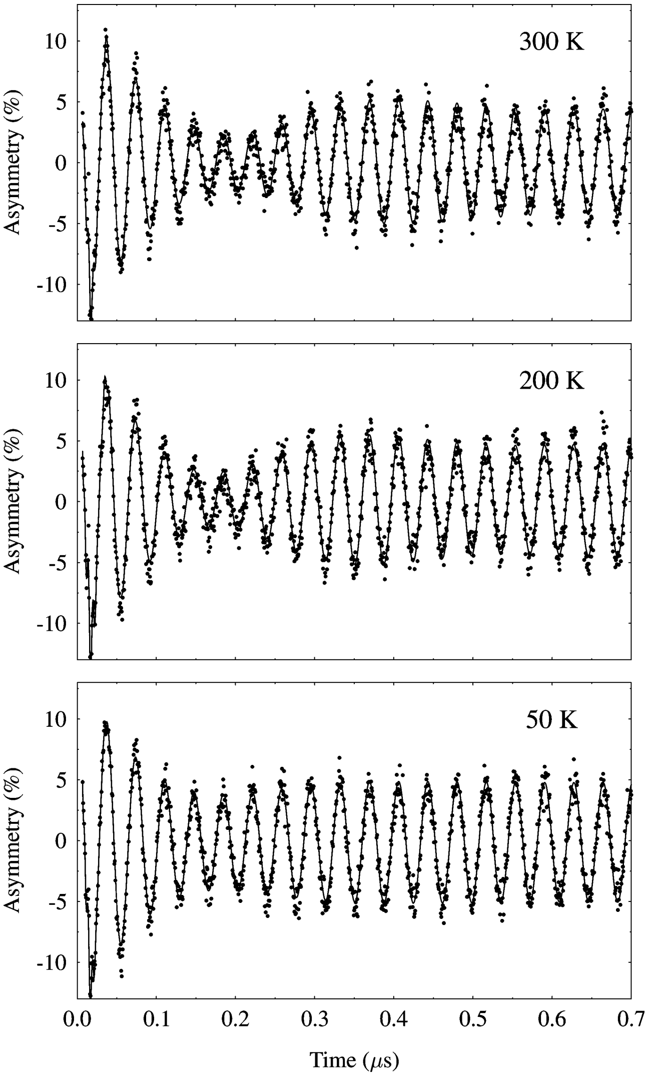

Figure 9. TF muon-spin-rotation signal for TTF in 0.2 T field at different temperatures. The solid lines show fitting to the sum of two radical muon-spin-rotation signals with hyperfine constants $A_1 \sim 300$ MHz and $A_2 \sim 5$ MHz, from ref 57.

with these data.[59] Moreover, the deepest region of negative electrostatic potential is found near the nitrogen atoms, making these attractive sites for muonium addition.[59] If the weaker feature is assigned to a proton Δ_0 resonance, a proton coupling of 43 MHz is obtained at 350 K. This proton-hyperfine coupling is again much larger than the scaled muon value, suggesting that the feature is in fact the Δ_1 resonance of a different radical with $A_\mu \sim 60$ MHz, most likely following the addition at a quinoidal carbon.[57]

Data taken for BEDT-TTF are more complex, with two strong, broad Δ_1 resonances at 0.85 T (230 MHz) and 1.05 T (280 MHz), whose relative strength is strongly temperature-dependent, and which are probably associated with the addition to the outer and inner C=C bonds, respectively.[57,59] There is also evidence for some very weakly coupled sites (1−10 MHz), which may correspond to the addition to the sulfur sites.[57]

It is clearly necessary to understand how these results transfer to studies on organic charge-transfer salts composed of these organic donors and acceptors.

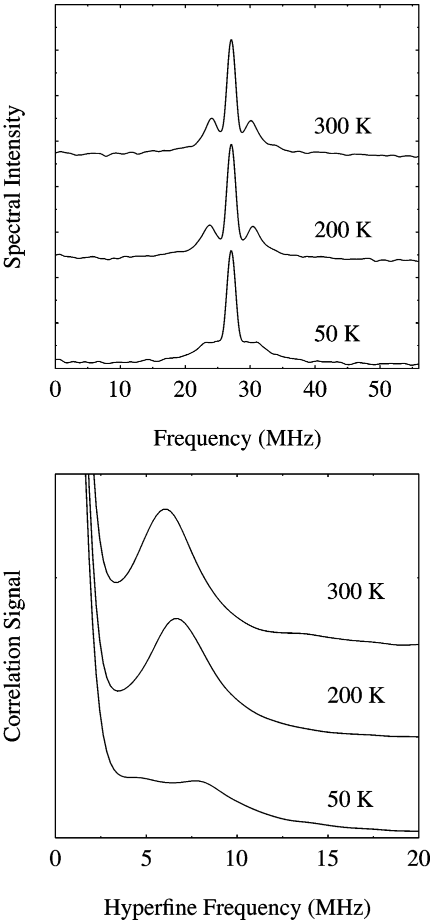

Figure 10. Upper panel shows the frequency spectrum of the 0.2 T TF muon-spin-rotation signal in TTF close to the diamagnetic frequency ($\gamma_\mu B$) at 28 MHz. Lower panel shows the corresponding radical frequency correlation spectrum, indicating a distinct state with hyperfine coupling around 5 MHz, from ref 57.

Calculations[59] show that the muon site is a sensitive function of electrostatic potential distribution and hence to the conformational energetics. The zero-point vibrational corrections to modes are also important in influencing the computed adduct couplings. Thus, the effect of the intermolecular packing in charge-transfer salts can be crucial. Muonium addition produces distortion in an organic molecule, and an unpaired electron can be left in the highest occupied molecular orbital of the distorted molecule. Nevertheless, the muoniated molecule can be thought of as a charge-neutral impurity; therefore, no major effect on the electronic band structure should be expected.

5. Organic Metals

Organic metals based upon charge-transfer salts of molecules such as those considered in the previous section have received much recent attention (see refs 53 and 60 for reviews of various aspects of this field). In muon studies of metallic organic salts, the Coulomb potential of the muon is strongly reduced by screening, so that bound muonium states are not possible. The probe here is then the diamagnetic muon. Muons are not directly sensitive to details of the metallic properties of organic metals, but they

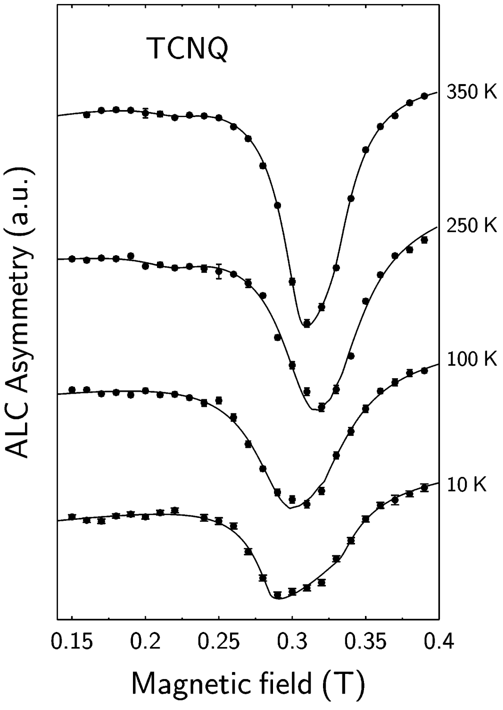

Figure 11. ALC spectrum for TCNQ as a function of temperature. The solid lines show fitting to a Δ_1 resonance around 0.3 T as the dominant feature with a very much weaker resonance becoming (only just) visible around 0.22 T in the higher temperature spectra, from ref 57.

can be used to probe features of the ground state. For example, in a number of these metallic charge-transfer salts, it is found that there is a competition between a spin-density wave (SDW) ground state and a superconducting ground state.[53] The superconducting state will be described in the next section, but the SDW state is also of great interest. If the muon occupies one site per unit cell and the SDW is commensurate with the crystal lattice, a number of distinct muon-spin precession frequencies would be expected to be measured. If the SDW is incommensurate, a Bessel function relaxation[61,62] is predicted if the field at the muon site varies sinusoidally, easily recognized because the maxima and minima appear shifted by a $\pi/4$ phase. The SDW state in $(TMTSF)_2X$, where X = PF_6, NO_3, and ClO_4, has been detected using μSR with similar amplitude for all three compounds.[61,62] The observed oscillations are consistent with an incommensurate SDW. In $(BEDT\text{-}TTF)_2KHg(SCN)_4$, a very weak SDW (of estimated amplitude $3 \times 10^{-3}\ \mu_B$) has been detected[63] below 12 K. This SDW state, too small to be seen by NMR, was suspected based on susceptibility and Fermi surface experiments[64,65] but showed up in μSR data as a small change in the zero-field spin relaxation. The low amplitude is consistent with a large on-site Coulomb interaction and small SDW gap[63] [even in the SDW state, $(BEDT\text{-}TTF)_2KHg(SCN)_4$ is a good metal]. However, there is now growing evidence that the ground state in $(BEDT\text{-}TTF)_2KHg(SCN)_4$ may in fact be a charge-density wave.[66,67] The most useful application of μSR in organic metals is however toward the superconducting state, which will be considered in the following section.

6. Organic Superconductors

To understand the usefulness of muons, recall that the two important length scales in superconductors are the penetration depth, λ, which controls the ability of the superconductor to screen magnetic fields, and the coherence length, ξ, which controls the length scale over which the order parameter can vary without undue energy cost. If the former is sufficiently greater than the latter (the condition is that $\lambda > \xi/\sqrt{2}$), the material is a type-II superconductor, which if cooled through its transition temperature, T_c, in an applied magnetic field (bigger than B_{c1}), it remains superconducting everywhere except in the cores of the superconducting vortices, which usually are arranged in a triangular lattice. Each vortex is associated with a magnetic flux equal to one flux quantum $\Phi_0 = h/2e$. The distance between vortices, d, is such that the number of vortices per unit area $2/(\sqrt{3}d^2)$ equals the number of flux quanta per unit area B/Φ_0. Thus, $d \propto B^{-1/2}$. (For a square vortex lattice, the number of vortices per unit area is $1/d^2$ and the relationship $d \propto B^{-1/2}$ holds.) In general, the vortex lattice will be incommensurate with the crystal lattice and, except at very high magnetic field, the vortex cores will be separated by a much larger distance than the unit-cell dimensions. Implanted muons will sit at certain crystallographic sites and thus will randomly sample the field distribution of the vortex lattice.

In the normal state ($T > T_c$) with a transverse field B, all muons precess with frequency $\omega = \gamma_\mu B$ (Figure 12a). In the superconducting state, however, the muons implanted close to the vortex cores experience a larger magnetic field than those implanted between vortices. Consequently, there is a spread in precession frequency, resulting in a progressive dephasing of the observed precession signal (Figure 12b). When the penetration depth becomes larger, the magnetic field variation becomes smaller and the dephasing becomes less pronounced (compare parts b and c of Figure 12). In fact, for the case of a perfect triangular

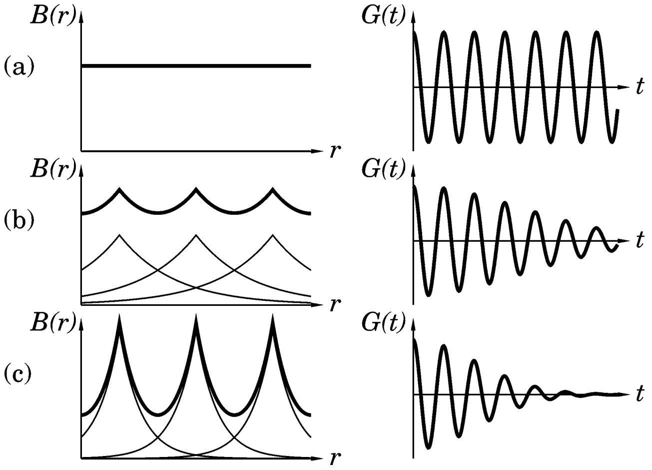

Figure 12. Schematic diagram of the magnetic field inside a superconductor as a function of the position and the corresponding muon-spin relaxation function, $G(t)$, for three cases: (a) the normal state, (b) the superconducting state, and (c) as b but with a shorter penetration depth.

vortex lattice, the relaxation rate σ of the observed precession signal is related to the penetration depth using

$$\sigma = \gamma_\mu \langle B(\boldsymbol{r}) - \langle B(\boldsymbol{r})\rangle_{\boldsymbol{r}}{}^{1/2}\rangle_{\boldsymbol{r}}{}^{1/2} \approx 0.0609\gamma_\mu \Phi_0/\lambda^2 \quad (18)$$

where $B(\boldsymbol{r})$ is the field at position $\boldsymbol{r}$ and the averages are taken over all positions.[68] Thus, the relaxation rate of the observed precession signal can be used to directly obtain the magnetic penetration depth. An advantage is that data are obtained from the bulk of the superconductor, in contrast to techniques involving microwaves, which are only sensitive to effects within a skin depth of the surface.

This principle has been applied to many different superconductors to extract both the penetration depth and its temperature dependence.[69] This latter quantity is of great interest because it is a measure of the temperature dependence of the order parameter and can yield information concerning the symmetry of the superconducting gap and hence the symmetry of the pairing mechanism (e.g., whether it is a *s* or *d* wave[70]). For example, this approach has revealed unconventional pairing in a sample of the high-temperature superconductor $YBa_2Cu_3O_{6+x}$.[71] In some cases, it is also possible to extract the vortex-core radius from a detailed analysis of the data.[72,73] μSR has also been used to detect weak static magnetism coexisting with superconductivity in $YBa_2Cu_3O_{6+x}$,[74,75] which may be associated with static fields in the vortex cores in underdoped samples.[76]

The field distribution $p(B)$ inside the superconductor is defined by $p(B) = \langle\delta(B - B(\boldsymbol{r}))\rangle_{\boldsymbol{r}}$ and is the probability that a randomly chosen point in the sample has a field B.[68] In general, the muon-spin relaxation function $G(t)$ is related to the field distribution $p(B)$ using

$$G(t) = \mathrm{Re}\langle \exp(i\gamma_\mu B(\boldsymbol{r})t)\rangle_{\boldsymbol{r}} = \mathrm{Re}\left(\int_{-\infty}^{\infty} p(B)e^{i\gamma_\mu \mathrm{Bt}}\, \mathrm{d}B\right), \quad (19)$$

and thus $G(t)$ can follow changes in $p(B)$ as both the temperature and applied field B_{applied} are varied.

A conventional type-II superconductor exhibits 3 well-defined phases for $T < T_c$: (1) a Meissner phase for $B_{\mathrm{applied}} < B_{c1}$, (2) a mixed or Shubnikov phase for $B_{c1} < B_{\mathrm{applied}} < B_{c2}$ (in which the magnetic field enters the superconductor in the form of well-defined flux lines or vortices arranged in a lattice) and (3) the normal metallic phase for $B_{\mathrm{applied}} > B_{c2}$. In highly anisotropic systems, the vortex lattice is no longer a system of rigid rods but should be considered as a system of flexible interacting lines. A useful picture is that of a weakly coupled stack of quasi-two-dimensional (q2D) “pancake” vortices, each one confined to a superconducting plane.[77,78] The phase diagram is thus substantially altered to take into account the field- and temperature-dependent changes in the vortex lattice itself. At low T and low B, the stacks resemble conventional vortex lines. Above a characteristic temperature T_b but still below that at which superconductivity is destroyed, the vortex lattice is broken up by thermal fluctuations[78] (this is called vortex-lattice melting). At low T but this time increasing B, the energetic cost of interlayer deformations of the lattice (local tilting of the lines) is progressively outweighed by the cost of intralayer deformations within the superconducting plane (shearing). Above a crossover field B_{cr}, the vortex lattice enters a more two-dimensional regime. Thus, in anisotropic systems, one may expect field- and temperature-dependent transitions in which the vortex lattice is destroyed. When muons are implanted into a superconductor in a field B_{applied}, one can directly measure the field distribution $p(B)$. This is shown in Figure 13a for an ideal vortex-line lattice. The distribution is highly asymmetric, with the high field “tail” corresponding to regions of the lattice close to the vortex cores (see Figure 13b). The maximum of the distribution occurs at B_{pk}, which lies below the mean field $\langle B\rangle$ (see Figure 13a). Such line shapes have been observed at low temperatures and fields in various anisotropic superconductors using μSR, including the high-temperature superconductors,[79] and, as will be discussed below, in organic superconductors.[80] In both cases, it is found that the vortex lattice can be melted with a temperature at T_b or can cross into a two-dimensional regime at fields above B_{cr}. Both transitions can be followed by measuring the field and temperature dependence of the $p(B)$ line shapes.

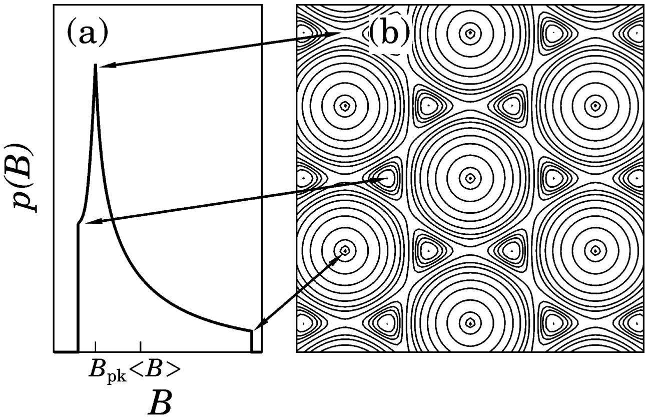

Figure 13. (a) Field distribution $p(B)$ in the vortex lattice (contours of B shown in b). The function $p(B)$ is essentially the Fourier transform of $G(t)$, according to eq 19.

Early μSR measurements on the organic superconductor κ-(BEDT-TTT)$_2$Cu(SCN)$_2$[81−83] produced contradictory results concerning the low-temperature behavior of the penetration depth $\lambda(T)$. These were all performed at rather large transverse fields, ~300−400 mT (to obtain a larger number of precessions during the muon lifetime), but in fact, this destroys the anisotropic vortex structure. Figure 14 is a μSR line shape measured at 1.8 K for a sample of κ-(BEDT-TTF)$_2$Cu(SCN)$_2$ showing the measured line shape cooled in a field of only 2.5 mT, which was derived from the muon time spectra using a maximum entropy technique.[79,84] The inset curve in Figure 14a is the probability distribution $p(B)$ from a numerical simulation of a vortex-line lattice in a uniaxial superconductor at an angle of 45° to the superconducting planes. The solid curve in the main part of Figure 14a is the convolution of this field distribution with instrumental and dipolar broadening of 0.23

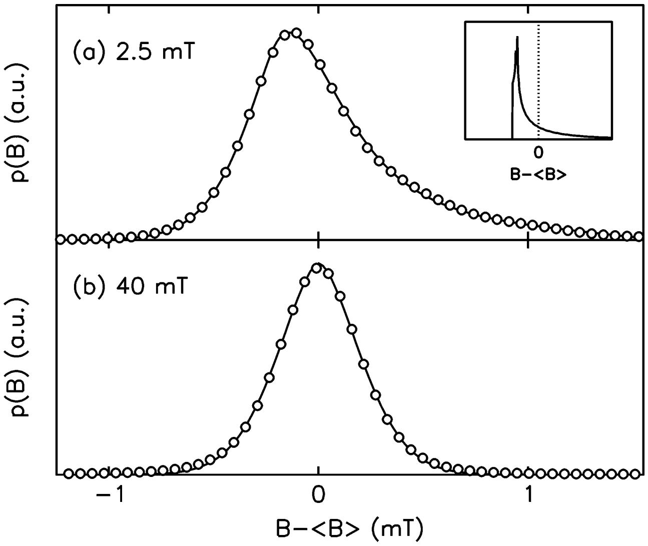

Figure 14. κ-(BEDT-TTT)$_2$Cu(SCN)$_2$ showing the measured line shape when field-cooled to 1.8 K in a field applied at 45° to the superconducting planes. The line shapes are obtained from transverse-field muon data (e.g., see the right-hand panels in Figure 12) by what amounts to Fourier transforming (although actually a maximum entropy technique is used). (a) At 2.5 mT, the characteristic asymmetric vortex-line-lattice shape is seen. [Note that the circles are data and the solid line is a simulation of the ideal vortex-line shape convolved with instrument response. The inset shows the computed $p(B)$ before convolution.] (b) At 40 mT, a symmetric line shape is obtained because of the 2D arrangement of pancake vortices, which results in a more symmetrical vortex field distribution.[80]

mT, which describes the data well. The long penetration depth in BEDT-TTF superconductors means that the field distribution because of the vortices is very narrow and is of the same order as the field distribution because of the nuclear dipoles. Moreover, the very low field used to ensure the existence of the vortex lattice means that it is essential to use a pulsed muon source such as ISIS because the very long time window available reduces the contribution from instrumental broadening.[85]

Figure 14b shows the μSR line shape taken for the same sample cooled in a larger field of 40 mT. The line shape is highly symmetric, with a mode at B_{pk} close to the average field $\langle B\rangle$. This change of the line shape with the field is very similar to changes observed in the high-T_c superconductor $\mathrm{Bi_2Sr_2CaCu_2O_{8+\delta}}$ (BSCCO) and indicates the loss of short-range correlations of the pancake vortices along the field direction.[79] It is attributed to the effective smearing out of the core fields because of the local tilt deformations of the pancake stacks.[79,86,87]

One can quantify the line shape by a dimensionless skewness parameter, β, appropriate for the very narrow line shapes that occur in κ-ET$_2$Cu(SCN)$_2$, which can be defined as

$$\beta = \frac{\langle B\rangle - B_{\mathrm{pk}}}{(\langle B^2\rangle - \langle B\rangle^2)^{1/2}}. \tag{20}$$

A value of $\beta = 0$ indicates a symmetric line shape, while a positive value reflects a weighting toward fields higher than B_{pk}, which is the case for a line shape arising from a vortex-line lattice (Figure 14a). As a function of the field, it is found that there is a broad crossover centered around $B_{\mathrm{cr}} \sim 7$ mT from the asymmetric line shape of Figure 14a to the almost symmetric line shape of Figure 14b.[80]

For $B > B_{\mathrm{cr}}$, the line width is very narrow and β is close to zero; $\langle \Delta B^2\rangle^{1/2}(T)$ is not inconsistent with that expected for a conventional *s*-wave superconductor. However, for $B < B_{\mathrm{cr}}$, there is a dramatic increase in the line width below $T^* \sim 5$ K (note that the superconducting transition temperature is 10.4 K). More significantly, the *line shape* also changes around T^*. While for $T < T^*$, the value of β approaches that expected for an ideal vortex-line lattice; this value falls rapidly with T and plateaus at a significantly reduced value. This reduction in β, reflecting a change in the line shape, indicates a reduction of pancake vortex correlations along the field direction. An estimate of the characteristic temperature for the thermally induced breakup of an electromagnetically coupled pancake stack is given by $T_{\mathrm{b}} = \phi_\circ^2 s/k_{\mathrm{B}}\mu_\circ(4\pi)^2 2\lambda_{\parallel}^2 \approx 4.5$ K,[78] where s is the interlayer spacing. The reduction in the positional correlations of pancake vortices at $T^* \sim 5$ K is thus consistent with this prediction.[80,85]

The crossover field B_{cr} is closely related to the "second-peak" effect, which has been observed in magnetization hysteresis loops.[88] For a Josephson-coupled superconductor ($\lambda_{\parallel} \gg \gamma s$) the dimensional crossover is expected at a field $B_{\mathrm{J}} \sim \phi_\circ/(\gamma s)^2$, when the width of the Josephson vortex core γs equals the vortex separation. (Here, s is the separation of the superconducting planes, $\gamma = \lambda_\perp/\lambda_\parallel$ is the superconducting anisotropy parameter, and $\lambda_\perp$ and $\lambda_\parallel$ are the superconducting penetration depths for currents flowing perpendicular and parallel, respectively, to the superconducting planes in a uniaxial system.) When the anisotropy is very large $\gamma s \gg \lambda_\parallel$, the rigidity of the vortex line is controlled by the tilt modulus of the lattice and is dominated by a highly dispersive electromagnetic interaction, so that despite long wavelength stiffness the vortices are subject to short wavelength fluctuations.[89,80] Electromagnetic coupling is believed to dominate in BSCCO[90,91] and κ-(BEDT-TTF)$_2$Cu(SCN)$_2$,[80,85] and taking the layer separation for κ-(BEDT-TTF)$_2$Cu(SCN)$_2$ as $s \sim 1.6$ nm yields an estimate $B_{\mathrm{cr}} \sim 7$ mT, which is in agreement with the μSR experiment.[80]

The field dependence of β at 2 K is shown in Figure 15a[92] and shows a crossover from a value consistent with a trangular Abrikosov vortex structure ($\beta = 0.60$) to a symmetric line shape. Flux decoration experiments have confirmed the presence of a triangular vortex lattice at fields below 1 mT.[93] The breakup of the interlayer order above 5 K is shown in the temperature dependence of β in Figure 15b. Extraction of the penetration depth below 3 mT (where the vortex lattice appears to be stable) reveals a linear term in $\lambda(T)$,[92] which is evidence for line nodes in the order parameter. Similar vortex lattice behavior is observed for other BEDT-TTF superconductors, such as β-(BEDT-TTF)$_2$IBr$_2$ and α-(BEDT-TTF)$_2$NH$_4$Hg(SCN)$_4$, which have varying degrees of anisotropy.[85,94]

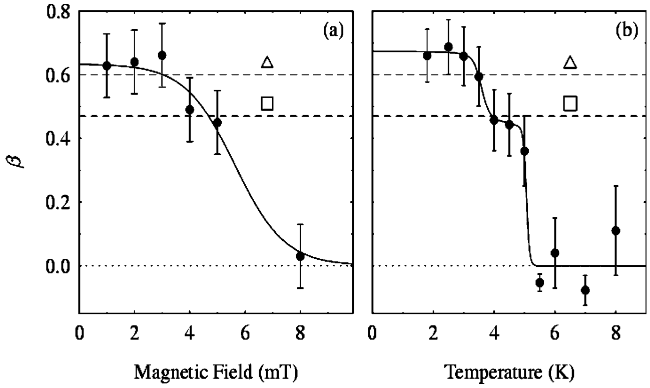

Figure 15. Measurements of β in κ-(BEDT-TTT)$_2$Cu(SCN)$_2$ for the field perpendicular to the BEDT-TTF layers. For this material, $T_{\text{[IMAGE]}} = 10.4$ K and $T^* \sim 5$ K. (a) Field dependence at 2 K and (b) temperature dependence in 3 mT.[92] Expected β are shown for triangular and square three-dimensional flux-line lattices.

μSR can also be used to study the field distribution inside *moving* vortex lattices, driven by a current. In this case, the muon-spin autocorrelation function $G(t)$ follows

$$G(t) = \mathrm{Re}\langle \exp(i\gamma_\mu \int_0^t B(r - vt')\,\mathrm{d}t')\rangle \qquad (21)$$

where v is the velocity of the vortex lattice. Experiments of this type in Pb−In give results that are in agreement with small angle neutron scattering[95] and can provide microscopic information on flux flow. To date, no analogous experiments have been performed on organic superconductors.

Recently, some interesting angle-dependent structures have been observed on the width of the internal field distribution in κ-(BEDT-TTF)$_2$Cu(SCN)$_2$, which may be connected with some instabilities of the titled vortex structure.[96]

The London formula for the zero temperature limit of the penetration depth $\lambda(0)$ yields in the clean limit (the mean free path much bigger than the coherence length) the relation: $\lambda(0) \propto \sqrt{m^*/n_s(0)}$, where m^* is the effective mass and $n_s(0)$ is the density of superconducting electrons. This can be combined with measurements of the Sommerfeld constant to yield a value for the Fermi temperature T_F. Thus, from muon measurements, it is possible to plot a diagram showing the relationship between the Fermi and critical temperatures for a range of superconductors.[97] This picture has come to be called a Uemura plot, shows a clear correlation between T_c and T_F for the heavy fermion, organic, fullerene, and Chevrel phase superconductors, and is equivalent to a scaling $T_c \propto \lambda^{-2}$. The conventional, elemental superconductors lie away from this correlation and have values of $T_c/T_F \sim 10^{-3}$ (for the "exotic" superconductors, this value is 1 or 2 orders of magnitude larger). This correlation has been interpreted as evidence that the exotic superconductors may be close to Bose−Einstein condensation of preformed local pairs, which is expected to occur at a temperature $\sim T_F$.[98] BEDT-TTF and the related BETS superconductors do follow this trend quite well, although there is some recent evidence that the correlation is closer to a $T_c \propto \lambda^{-3}$ behavior,[99,100] and this may be connected with theoretical models that predict a departure from Uemura scaling.[101,102] (The molecule BETS, also known as BEDT-TSF, is related to BEDT-TTF and may be obtained by replacing the innermost 4 sulfur atoms of BEDT-TTF with selenium. The selenium atoms are larger than the sulfur atoms and tend to broaden the electronic bands.)

The interplay between coexisting magnetism and superconductivity is an important topic, and the salts κ-BETS$_2$FeBr$_4$ and κ-BETS$_2$FeCl$_4$ are of interest in this context. In these crystals, sheets of dimers of BETS molecules alternate with layers of magnetic anions. The spatial separation of the highly conducting molecular layers and the strongly magnetic layers is a key feature of this structure. Magnetic and transport measurements on the FeBr$_4$ salt indicate that the Fe^{3+} is in a high-spin state ($S = 5/2$) with an antiferromagnetic transition at $T_N = 2.5$ K and a superconducting transition taking place at $T_c = 1$ K.[103] Zero-field muon-spin relaxation measurements on the organic metal κ-BETS$_2$FeCl$_4$ clearly show the formation of an antiferromagnetically ordered state below $T_N = 0.45$ K.[104] The magnetic order remains unperturbed on cooling through the superconducting transition $T_c \sim 0.17$ K, providing unambiguous evidence for the coexistence of antiferromagnetic order and superconductivity in this system. The internal field seen at a muon site depends on its position with respect to the magnetic structure, and hence a number of different frequencies are to be expected from the large low-symmetry unit cell of this material. Two clear precession frequencies are observed.[104] The antiferromagnetic nature of the Fe ordering means that high local fields such as reflected by the higher frequency can only be present close to the anion plane. For the lower frequency, sites arranged between FeCl$_4$ along the c axis are a possibility; however, the local field in the region around the center of the BETS sheets is also found to be consistent.[104] Superconductivity is expected to modify the SDW; therefore, the small drop in frequency seen on entering the superconducting state for the lower field site may provide evidence for the presence in the normal state of a weak SDW within the BETS layers, as previous calculations have suggested.[105] Similar behavior is found for κ-BETS$_2$FeBr$_4$, although the temperature dependence of the individual precession components is more difficult to extract.[99]

A new understanding of the phase diagram of the κ-phase BEDT-TTF family of salts has begun to emerge from a dynamical mean-field theory treatment of the Hubbard model on an anisotropic triangular lattice.[106] One of the key features to emerge from this model is a new energy scale T_0 (typically $\sim$30 K), which is much less than U or the bandwidth and is analogous to a Kondo temperature in the impurity model. The idea is that at low temperatures ($T < T_0$) there are local moments in the system (because of the proximity to the Mott insulating state) that are screened by the conduction electrons. Superconductivity can result if the electronic correlations are not so large that the Mott insulating state forms (i.e., the pressure is sufficiently large). At a high temperature, $T > T_0$, the local moments will be unscreened, but they will not be ordered because the exchange coupling between them will be relatively weak compared with T. It is hoped that muon measurements in the normal state of various organic superconductors may shed light on this problem.[107]

The salt $(TMTSF)_2ClO_4$ and related compounds have received much experimental interest because of their remarkably complex phase diagram.[108] μSR experiments on the superconducting phase of $(TMTSF)_2ClO_4$, which is believed to be unconventional (because of the absence of a Hebel–Slichter peak in the NMR $1/T_1$ and the sensitivity of T_c to the parts per million level of nonmagnetic impurities), found no spontaneous magnetic fields,[109] which would have been evidence for broken time-reversal symmetry, as found in experiments on various other unconventional superconductors.[110–112] The vortex lattice can nevertheless be detected and some preliminary studies of this have been performed.[109,113]

The family of 3D molecular superconductors based on doping C_{60} with alkali metals (A_xC_{60}, where A = Li, Na, K, Rb, Cs, or their mixtures)[114,115] have been studied using μSR.[116,117] The measured penetration depth, obtained by studying the muons that form diamagnetic states, of these compounds yields a correlation between T_c and T_F, consistent with the other exotic superconductors discussed above.[116] A fraction (~15%) of muons implant as endohedral muonium (muonium trapped inside the cage). An elegant study has measured the relaxation of this fraction in Rb_3C_{60}; the relaxation is due to the spin exchange scattering of endohedral muonium with thermal electronic excitations across the gap and a Hebel–Slichter coherence peak is observed at T_c,[35,117] consistent with the BCS weak coupling limit. The unpaired electron in the muonium enhances the sensitivity of the muon to these electronic excitations.

Another family is based on AC_{60} (where A = Rb[118,119] and Cs[120]) and has a more quasi-one-dimensional structure. These so-called alkali fulleride linear-chain polymers do not superconduct, and μSR experiments show random static magnetic order freezing at low temperatures;[118–120] there is a large distribution of internal fields in the magnetic ground state, which could be consistent with a SDW. However, more recent measurements using NMR[121,122] and antiferromagnetic resonance[123] have demonstrated that these materials have an antiferromagnetic ground state, although at higher temperatures, there are strong antiferromagnetic fluctuations suggesting a one-dimensional character. The ordered state may be incommensurate, which would explain the absence of a detection of order by μSR experiments.

7. Conducting Polymers

Before considering conducting polymers, it is worthwhile to understand the measurements that can be made on a nonconducting polymer such as polybutadiene. Figure 16 shows transverse-field μSR data for polybutadiene. The diamagnetic precession frequency ν_μ is clearly visible, together with artifacts (labeled c) from the cyclotron at 50, 100, and 200 MHz. The two additional frequencies, labeled ν_1 and ν_2, are due to the hyperfine coupling with the radical electron (cf. eq 16), and the correlation spectrum (cf. eq 17) shown in Figure 17 allows an extraction of the temperature dependence of the hyperfine coupling. At high temperatures, a strong narrow signal is observed, because of efficient dynamical orientational averaging of the hyperfine anisotropy.[124] On cooling, the lines become broader as the polymer dynamics slow.

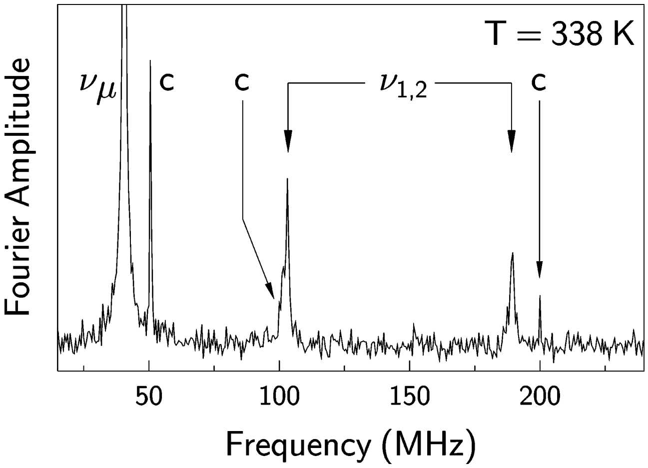

Figure 16. FFT of transverse-field μSR data for polybutadiene with a field of 0.3 T, after ref 125.

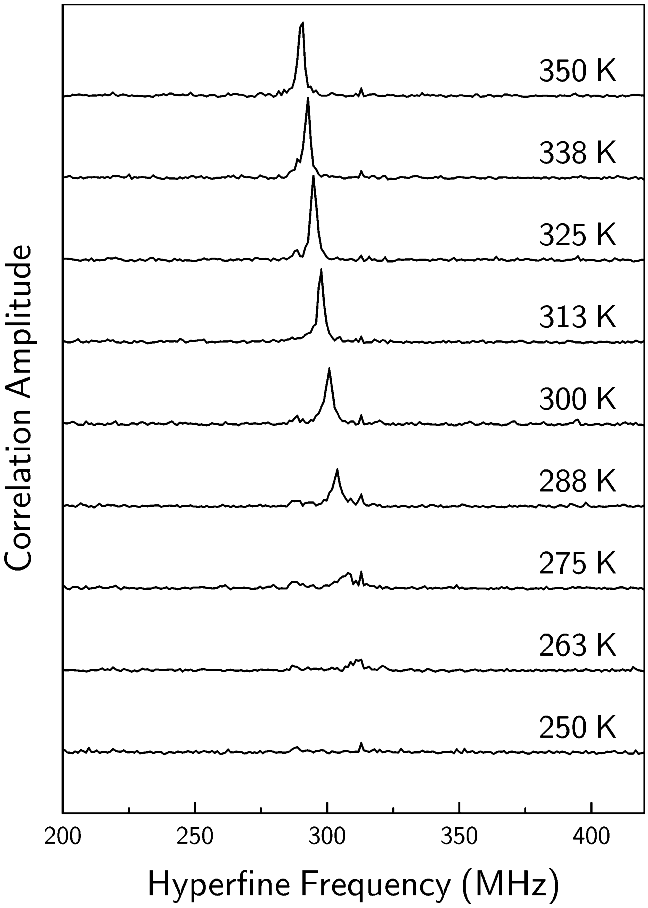

Figure 17. Associated correlation spectrum for polybutadiene. The hyperfine frequency decreases slightly on warming, after ref 125.

Similar behavior is seen for the $\Delta M = 0$ transition in the ALC spectrum (see Figure 18), but the $\Delta M = 1$ transition shows the opposite behavior, because it requires some residual anisotropy for oscillator strength. For $T \leq 225$ K, all of the radical signals become too broad to extract reliably from the background.[124,125] The dynamics close to the glass transition at 165 K can be followed using longitudinal-field μSR.[124] Similar effects are found for polystyrene.[126]

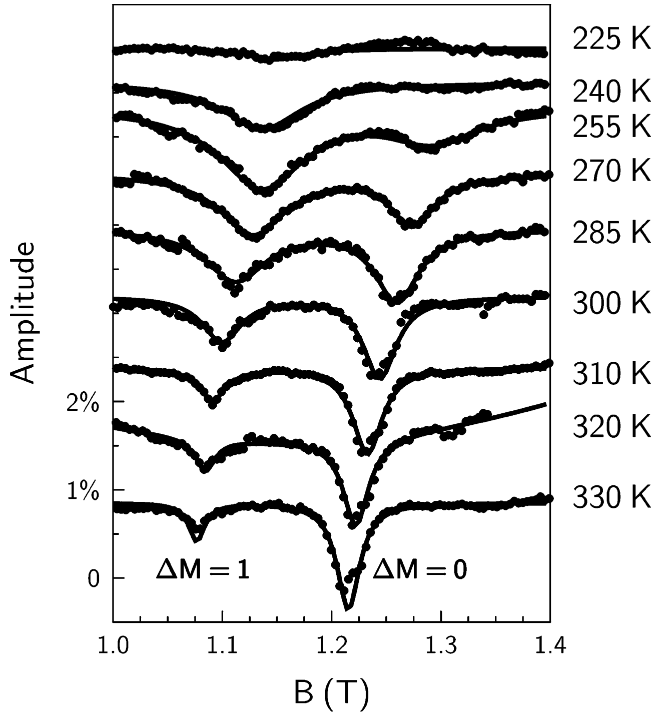

Figure 18. ALC data for polybutadiene, after ref 125.

However, the main point to be made about polybutadiene is that the muoniated radical is highly localized (see Figure 19), because the double bonds are separated from one another by polyethylene segments. Any modulation of the hyperfine coupling arises therefore from polymer motion. This is not the case for conducting polymers.

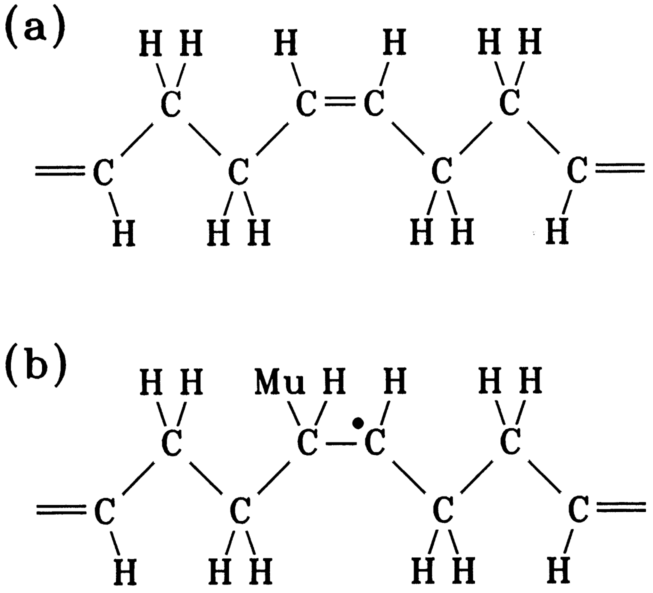

Figure 19. (a) Raw polybutadiene and (b) muoniated radical state.

Conducting polymers have attracted interest from a fundamental point of view because of the different types of mobile defects that can be found in them, including solitons[127] and polarons.[128,129] The reaction between muonium and *trans*-polyacetylene[130−134] produces a diamagnetic, neutral muon defect and a highly mobile unpaired spin (a soliton, see Figure 20).

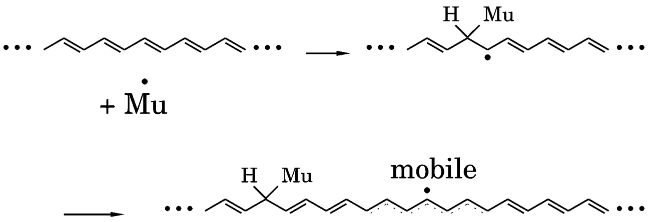

Figure 20. Muonium interaction with *trans*-polyacetylene to produce a diamagnetic radical and a mobile neutral soliton.

Because the unpaired spin is mobile, the hyperfine coupling between it and the muon defect is intermittent.[135] In other polymers, such as polyaniline (PANI) or polyphenylvinylene (PPV), the muon-induced defect is a negatively charged polaron.[136,137] In each case, the excitation diffuses up and down the chain but cannot cross the point at which the muon is bonded to the chain, which therefore acts as a barrier. Every time the excitation briefly revisits the muon, the muon−electron-hyperfine coupling is turned on and then off, so that successive visits progressively relax the muon polarization. A measurement of the magnetic field dependence of this relaxation yields the spectral density function associated with the excitation random walk and can be used to infer the dimensionality of the diffusion.[130,138] This occurs because the relaxation rate is connected with the noise power (or spectral density), $J(\omega_\mu)$, in the fluctuating magnetic field at the muon Larmor frequency, $\omega_\mu = \gamma_\mu B$, associated with that particular magnetic field B, where γ_μ is the muon gyromagnetic ratio. Sweeping the magnetic field allows one to extract the frequency distribution of the fluctuations over a range determined by the magnetic field. In fact, the situation is often a little more complicated because the main source of the muon relaxation is an intermittent hyperfine coupling so there is also a term that depends on the noise power at the electron Larmor frequency $\omega_e = \gamma_e B$. For diffusive motion along a polymer chain, the longitudinal relaxation rate may be written as

$$\lambda(B) \propto 3D^2 f(\omega_\mu) + (5A^2 + 7D^2) f(\omega_e) \qquad (22)$$

where A and D are the scalar and dipolar hyperfine-coupling parameters and $f(\omega_\mu)$ is the spectral density of the spin correlation function.[139,140]

Polaronic motion in *doped* conducting polymers can of course be measured using NMR and ESR;[141] for these techniques, the motional line-width contributions are proportional to the carrier density, and therefore measurements on conducting polymers are restricted to doped materials (e.g., see ref 142). Muons are uniquely sensitive to polaron transport in *undoped* materials (in which there is no significant carrier density to provide an NMR or ESR signal). In contrast to transport experiments, which provide results that are inevitably dominated by the slowest component of the transport process, muon measurements can provide information on the intrinsic transport processes governing the mobility of an electronic excitation along a chain.[143]

Measured muon relaxation data can be fit using the theory of Risch and Kehr[144] for a muon interacting through hyperfine-coupling ω_0 to the spin density on the chain site to which it is bonded (this is illustrated in Figure 21). In this model, when the hyperfine coupling is switched on, the muon electron system evolves according to a Hamiltonian given by eq 6 with $A = \omega_0$. When the hyperfine coupling is switched off, the electron and muon spins are decoupled and separately evolve according to the Zeeman terms in the Hamiltonian. In addition, the electron spin is subject to random spin flips at a rate λ. The fluctuating spin density induced by an electronic spin defect rapidly diffusing up and down the 1D chain leads to a relaxation function of the form $G(t) = \exp(\Gamma t)\ \mathrm{erfc}(\sqrt{\Gamma t})$ for $\lambda t_{\max} \gg 1$, with erfc signifying the complementary error function, $t_{\max}$, the experimental time scale, and Γ, a relaxation parameter. For $D_{\parallel} > \omega_0 > \lambda$, Γ has an inverse magnetic field dependence given by

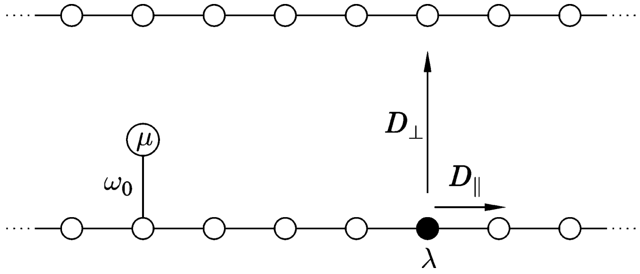

Figure 21. Schematic diagram of the polaron diffusion model used in the text, which is based on that of Risch and Kehr but includes interchain diffusion (after ref 124). The muon interacts through hyperfine-coupling ω_0 to the spin density on the chain site to which it is bonded. The electronic spin defect (black filled circle) rapidly diffuses up and down the chain with intra- and interchain diffusion rates $D_\parallel$ and $D_\perp$, respectively. λ is the electron spin-flip rate, assumed faster than the reciprocal of the experimental time scale.

$$\Gamma = \frac{\omega_0^4}{2\omega_e D_\parallel^2}. \tag{23}$$

The delocalization of the electronic defect in the neighborhood of the attached muonium is not known, but a neutral spin-$^1/_2$ defect is believed to be delocalized over six lattice constants in finite *trans*-polyacetylene based on calculations.[145] In the Risch–Kehr model, the Brownian motion of an extended defect is replaced by an effective hopping process of a localized defect.[144] (For a detailed discussion, see ref 140.)

Data for polyaniline[143] and various derivates of PPV[146] fit to the Risch–Kehr model very well, and the measured temperature dependence of Γ as a function of the field allow the extraction $D_\parallel$, using eq 23. The extracted $D_\parallel$ is then fit well by a simple model for the transport in which $D_\parallel \propto (\Sigma_0 + \Sigma_{\mathrm{ph}})^{-1}$, where Σ_0 is a temperature-independent-scattering term and Σ_{ph} is a phonon-scattering term proportional to the number of modes excited; therefore, it is proportional to $(\exp(E_{\mathrm{ph}}/k_B T) - 1)^{-1}$, where E_{ph} is the energy of a phonon mode. A scattering contribution proportional to the phonon number is expected in theories of phonon-limited polaron transport.[147,148] In each case, the energy of the phonon mode is found to be in agreement with a mode associated with whole chain librations or mixed chain torsions and ring librations, which have been observed in inelastic neutron scattering.[143,146] These data are shown in Figure 22 for two derivatives of PPV.

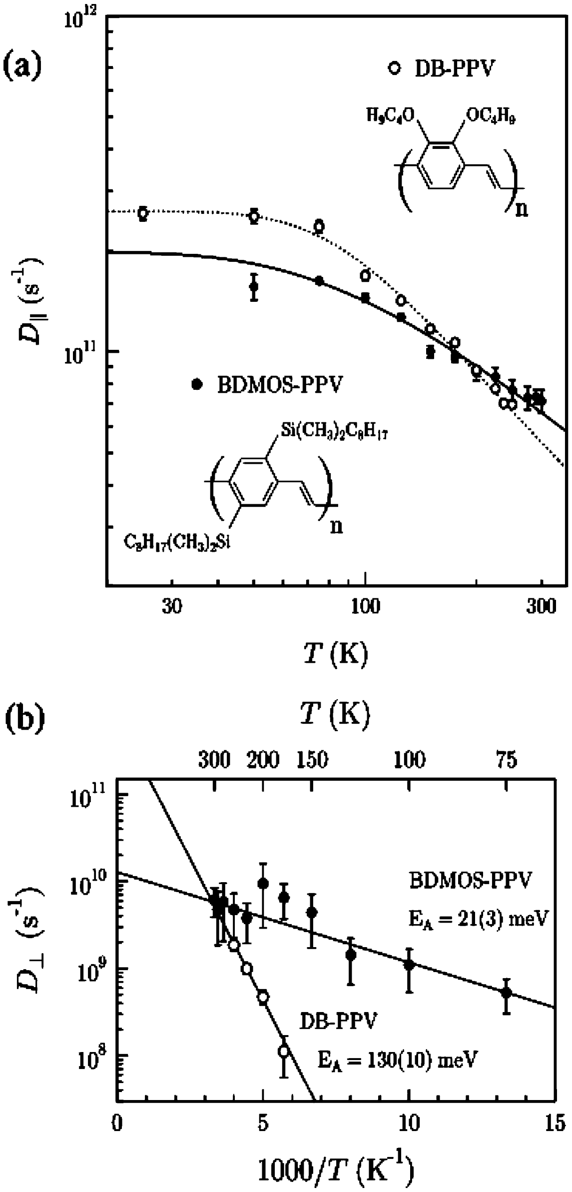

Figure 22. (a) Temperature dependence of the intrachain polaron diffusion rates in DB–PPV and BDMOS–PPV derived from the muon-spin relaxation. The main figure shows $D_\parallel$, and the solid line is a fit to a simple model of the transport, with a phonon activation energy of 22 meV (DB–PPV) or 11 meV (BDMOS–PPV). (b) Activated plot of the interchain diffusion rate $D_\perp$ for the two polymers. The fitted activation energies are 130(10) meV and 21(3) meV.[126,146]

The field B_c, at which crossover to a 3D diffusion regime is observed, can be used to estimate the interchain diffusion $D_\perp \approx \gamma_e B_c$. The interchain transport is assisted by thermal motion, rather than hindered by it, so that $D_\perp$ increases with increasing temperature (usually with an activated dependence), while $D_\parallel$ decreases.

The Risch–Kehr formalism has been very successful for understanding μSR data in conducting polymers and for extracting the inter- and intrachain diffusion rates. The model assumes a polymer of infinite extent; therefore, there is much interest in studying the effect of chain ends, both from a theoretical and experimental point of view. β-Carotene is an attractive material to study in this context because it can be regarded as a short-chain version of polyacetylene.[149] Another development in this area is the use of the formalism to describe conducting polymers in understanding the behavior of muons in bio-organic molecules.[150]

8. Slow Muons

All of the experiments described in this review so far have been on bulk samples, mainly using 4 MeV "surface" muons, which penetrate $\sim 10^{-4}$ m into most solid samples. Surface studies are beginning to be possible following the development of "slow muon" beams in which the energy of the muon beam is reduced down to $\sim$1–10 eV. This is achieved by either moderation in thin layers of rare gas solid[151,152] or also by resonant ionization of thermal muonium (μ^+e^- produced from the surface of a hot tungsten foil placed in a pulsed proton beam) by a pulsed laser source.[153] The efficiency of both of these processes is rather low, but the first method has proven to be particularly useful for doing experiments. Highlights of this technique include measurements of superparamagnetism in thin films,[154] magnetization in a trilayer,[155] the direct measurement of the penetration depth in a surface region of a superconductor,[156] measurements of the flux lattice,[157] and the direct observation of nonlocal effects in a superconducting film.[158] This is an exciting advance, and a promising area for future development is the use of slow muons for studying thin films of molecular conductors.

9. Conclusions

This review has given an outline of the variety of information that can be obtained using the μSR technique in its various guises. The muon is an extremely versatile probe, and with the extraordinary richness of behavior found for molecular conductors and related materials, it seems likely that the use of muons in studying such systems will remain extremely interesting, valuable, and full of surprises.

10. Acknowledgments

I am deeply indebted to my collaborators, both past and present, in the Oxford muon group and elsewhere, who have participated in the μSR work on organic and molecular conductors, and particularly to Dr Francis Pratt (RAL). I would also like to record my gratitude to the staff of the ISIS Pulsed Muon Facility and the Swiss Muon Source at the Paul Scherrer Institute in Villigen, Switzerland, for their expert technical support, and to the many chemists who have been kind enough to supply my group with excellent samples.

11. References

(1) Cox, S. F. J. *J. Phys. C* **1987**, *20*, 3187.
(2) Schenck, A. *Muon Spin Rotation Spectroscopy*, Adam Hilger, New York, 1985.
(3) Schenck, A.; Gygax, F. N. In *Handbook of Magnetic Materials*; K. H. J. Buschow, Ed.; Vol. 9, Elsevier: Amsterdam, The Netherlands, 1995.
(4) Dalmas de Réotier, P.; Yaouanc, A. *J. Phys. C* **1997**, *9*, 9113.
(5) Blundell, S. J. *Contemp. Phys.* **1999**, *40*, 175.
(6) Cottrell, S. P.; Cox, S. F. J.; Scott, C. A.; Lord, J. S. *Physica B* **2000**, *289*, 693.
(7) Arseneau, D. J.; Hitti, B.; Kreitzman, S. R.; Whidden, E. *Hyperfine Interact.* **1997**, *106*, 277.
(8) Abela, R.; Baines, C.; Donath, X.; Herlach, D.; Maden, D.; Reid, I. D.; Renker, D.; Solt, G.; Zimmermann, U. *Hyperfine Interact.* **1994**, *87*, 1105.
(9) Eaton, G. H.; Scott, C. A.; Williams, W. G. *Hyperfine Interact.* **1994**, *87*, 1099.
(10) Eaton, G. H.; Clarkegayther, M. A.; Scott, C. A.; Uden, C. N.; Williams, W. G. *Nucl. Instrum. Methods Phys. Res., Sect. A* **1994**, *342*, 319.
(11) King, P. J. C.; Cottrell, S. P.; Cox, S. F. J.; Eaton, G. H.; Hillier, A. D.; Lord, J. S.; Pratt, F. L.; Lancaster, T.; Blundell, S. J. *Physica B* **2003**, *326*, 260.
(12) Nagamine, K.; Matsuzaki, T.; Ishida, K.; Watanabe, I.; Kadono, R.; Eaton, G. H.; Jones, H. J.; Thomas, G.; Williams, W. G. *Hyperfine Interact.* **1994**, *87*, 1091.
(13) Matsuzaki, T.; Ishida, K.; Nagamine, K.; Watanabe, I.; Eaton, G. H.; Williams, W. G. *Nucl. Instrum. Methods Phys. Res., Sect. A* **2001**, *465*, 365.
(14) Nagamine, K. *Hyperfine Interact.* **1981**, *8*, 787.
(15) Miyake, Y.; Nishiyama, K.; Makimura, S.; Kawamura, N.; Shimomura, K.; Kadono, R.; Higemoto, W.; Fukuchi, K.; Beveridge, J. L.; Ishida, K.; Matsuzaki, T.; Watanabe, I.; Matsuda, Y.; Sakamoto, S.; Nakamura, S. N.; Nagamine, K. *Physica B* **2003**, *326*, 255.
(16) Hayano, R. S.; Uemura, Y. J.; Imazato, J.; Nishida, N.; Yamazaki, T.; Kubo, R. *Phys. Rev. B* **1979**, *20*, 850.
(17) Amato, A. *Rev. Mod. Phys.* **1997**, *69*, 1119.
(18) Keren, A.; Mendels, P.; Campbell, I. A.; Lord, J. *Phys. Rev. Lett.* **1996**, *77*, 1386.
(19) Blundell, S. J.; Pratt, F. L.; Lancaster, T.; Marshall, I. M.; Steer, C. A.; Heath, S. L.; Létard, J. F.; Sugano, T.; Mihailovic, D.; Omerzu, A. *Polyhedron* **2003**, *22*, 1973.
(20) Blundell, S. J. In *Magnetism: Molecules to Materials*; Miller, J. S., Drillon M., Eds.; Wiley-VCH: Weinheim, Germany, 2001; pp 235–256.
(21) Blundell, S. J.; Pratt, F. L. *J. Phys.: Condens. Matter* **2004**, *16*, R771.
(22) Ahmed, S. N.; Anthony, A. E.; Beier, E. W.; Bellerive, A.; Biller, S. D.; Boger, J.; Boulay, M. G.; Bowler, M. G.; Bowles, T. J.; Brice, S. J.; Bullard, T. V.; Chan, Y. D.; Chen, M.; Chen, X.; Cleveland, B. T.; Cox, G. A.; Dai, X.; Dalnoki-Veress, F.; Doe, P. J.; Dosanjh, R. S.; Doucas, G.; Dragowsky, M. R.; Duba, C. A.; Duncan, F. A.; Dunford, M.; Dunmore, J. A.; Earle, E. D.; Elliott, S. R.; Evans, H. C.; Ewan, G. T.; Farine, J.; Fergani, H.; Fleurot, F.; Formaggio, J. A.; Fowler, M. M.; Frame, K.; Frati, W.; Fulsom, B. G.; Gagnon, N.; Graham, K.; Grant, D. R.; Hahn, R. L.; Hall, J. C.; Hallin, A. L.; Hallman, E. D.; Hamer, A. S.; Handler, W. B.; Hargrove, C. K.; Harvey, P. J.; Hazama, R.; Heeger, K. M.; Heintzelman, W. J.; Heise, J.; Helmer, R. L.; Hemingway, R. J.; Hime, A.; Howe, M. A.; Jagam, P.; Jelley, N. A.; Klein, J. R.; Kos, M. S.; Krumins, A. V.; Kutter, T.; Kyba, C. C. M.; Labranche, H.; Lange, R.; Law, J.; Lawson, I. T.; Lesko, K. T.; Leslie, J. R.; Levine, I.; Luoma, S.; MacLellan, R.; Majerus, S.; Mak, H. B.; Maneira, J.; Marino, A. D.; McCauley, N.; McDonald, A. B.; McGee, S.; McGregor, G.; Mifflin, C.; Miknaitis, K. K. S.; Miller, G. G.; Moffat, B. A.; Nally, C. W.; Neubauer, M. S.; Nickel, B. G.; Noble, A. J.; Norman, E. B.; Oblath, N. S.; Okada, C. E.; Ollerhead, R. W.; Orrell, J. L.; Oser, S. M.; Ouellet, C.; Peeters, S. J. M.; Poon, A. W. P.; Robertson, B. C.; Robertson, R. G. H.; Rollin, E.; Rosendahl, S. S. E.; Rusu, V. L.; Schwendener, M. H.; Simard, O.; Simpson, J. J.; Sims, C. J.; Sinclair, D.; Skensved, P.; Smith, M. W. E.; Starinsky, N.; Stokstad, R. G.; Stonehill, L. C.; Tafirout, R.; Takeuchi, Y.; Tesic, G.; Thomson, M.; Thorman, M.; Van Berg, R.; Van de Water, R. G.; Virtue, C. J.; Wall, B. L.; Waller, D.; Waltham, C. E.; Tseung, H. W. C.; Wark, D. L.; West, N.; Wilhelmy, J. B.; Wilkerson, J.

F.; Wilson, J. R.; Wittich, P.; Wouters, J. M.; Yeh, M.; Zuber, K. *Phys. Rev. Lett.* **2004**, *92*, 102004.
(23) Chappert, J. *Muons and Pions in Materials Research*; Chappert, J., Grynszpan, R. I., Eds.; Elsevier: Amsterdam, The Netherlands, 1984.
(24) Garwin, R. L.; Lederman L. M.; Weinrich M. *Phys. Rev.* **1957**, *105*, 1415.
(25) Pratt, F. L. *Philos. Mag. Lett.* **1997**, *75*, 371.
(26) Cox, S. F. J. *J. Phys.: Condens. Matter* **2003**, *15*, R1727.
(27) Cox, S. F. J.; Symons, M. C. R. *Chem. Phys. Lett.* **1986**, *126*, 516.
(28) Patterson, B. D. *Rev. Mod. Phys.* **1988**, *60*, 69.
(29) Chow, K. H.; Lichti, R. L.; Kiefl, R. F.; Dunsiger, S.; Estle, T. L.; Hitti, B.; Kadono, R.; MacFarlane, W. A.; Schneider, J. W.; Schumann, D.; Shelley, M. *Phys. Rev. B* **1994**, *50*, 8918.
(30) Chow, K. H.; Hitti, B.; Kiefl, R. F. *Semicond. Semimet.* **1998**, *51A*, 137.
(31) Hartmann, O. *Hyperfine Interact.* **1979**, *6*, 47.
(32) Johnston, T. M. S.; Chow, K. H.; Dunsiger, S.; Duty, T.; Kiefl, R. F.; Koster, E.; MacFarlane, W. A.; Morris, G. D.; Sonier, J.; Williams, D. L. I. *Hyperfine Interact.* **1997**, *106*, 71.
(33) Cox, S. F. J.; Cottrell, S. P.; Charlton, M.; Donnelly, P. A.; Ewels, C.; Heggie, M.; Hourahine, B. *J. Phys.: Condens. Matter* **2001**, *13*, 2169.
(34) Blundell, S. J.; Cox, S. F. J. *J. Phys.: Condens. Matter* **2001**, *13*, 2163.
(35) MacFarlane, W. A.; Kiefl, R. F.; Dunsiger, S.; Sonier, J. E.; Chakhalian, J.; Fischer, J. E.; Yildirim, T.; Chow, K. H. *Phys. Rev. B* **1998**, *58*, 1004.
(36) Kiefl, R. F.; Schneider, J. W.; MacFarlane, A.; Chow, K.; Duty, T. L.; Estle, T. L.; Hitti, B.; Lichti, R. L.; Ansaldo, E. J.; Schwab, C.; Percival, P. W.; Wei, G.; Wlodek, S.; Kojima, K.; Romanow, W. J.; McCauley, J. P.; Coustel, N.; Fischer, J. E.; Smith, A. B. *Phys. Rev. Lett.* **1992**, *68*, 2708.
(37) Roduner, E. *Chem. Soc. Rev.* **1993**, *22*, 337.
(38) Reid, I. D.; Azuma, T.; Roduner, E. *Nature* **1990**, *345*, 328.
(39) Lovett, B. W.; Blundell, S. J.; Stiessberger, J.; Pratt, F. L.; Jestadt, T.; Cottrell, S. P.; Reid, I. D. *Phys. Rev. B* **2001**, *63*, 054204.
(40) Cox, S. F. J.; Sivia, D. S. *Appl. Magn. Reson.* **1997**, *12*, 213.
(41) Cox, S. F. J. *Solid State Nucl. Magn. Reson.* **1998**, *11*, 103.
(42) Heming, M.; Roduner, E.; Patterson, B. D.; Odermatt, W.; Schneider, J.; Baumeler, H.; Keller, H.; Savic, I. M. *Chem. Phys. Lett.* **1986**, *128*, 100.
(43) Kiefl, R. F.; Kreitzman, S.; Celio, M.; Keitel, R.; Luke, G. M.; Brewer, J. H.; Noakes, D. R.; Percival, P. W.; Matsuzaki, T.; Nishiyama, K. *Phys. Rev. A* **1986**, *34*, 681.
(44) Kreitzman, S. R. *Hyperfine Interact.* **1986**, *31*, 13.
(45) Kiefl, R. F. *Hyperfine Interact.* **1986**, *32*, 707.
(46) Tregenna-Piggott, P. L. W.; Roduner, E.; Santos, S. *Chem. Phys. Lett.* **1996**, *203*, 317.
(47) Wangsness, R. K.; Bloch, F. *Phys. Rev.* **1953**, *89*, 729.
(48) Nosov, V. G.; Yakovleva I. V. *Sov. Phys. JETP* **1963**, *16*, 1236.
(49) Meier, P. F. *Phys. Rev.* **1982**, *A25*, 1287.
(50) Roduner, E.; Strub, W.; Burkhard, P.; Hochmann, J.; Percival, P. W.; Fischer, H.; Ramos, M.; Webster, B. C. *Chem. Phys.* **1982**, *67*, 275.
(51) Percival, P.; Roduner, E.; Fischer, H *Chem. Phys.* **1978**,*32*, 353.
(52) Fisher, A. J. *Curr. Opin. Solid State Mater. Sci.* **1996**, *1*, 841.
(53) Ishiguro T.; Yamaji K.; Saito G. *Organic Superconductors*; Springer-Velag: Berlin, Germany, 1998.
(54) Day, P. *Phys. Scr., T* **1993**, *49*, 726.
(55) Singleton, J. *Rep. Prog. Phys.* **2000**, *63*, 1111.
(56) Wosnitza, J. *Fermi Surfaces of Low-Dimensional Organic Metals and Superconductors*; Springer-Verlag: Berlin, Germany, 1996.
(57) Pratt, F. L.; Blundell, S. J.; Jestädt, T.; Lovett, B. W.; Macrae, R. M.; Hayes, W. *Magn. Reson. Chem.* **2000**, *38*, S27.
(58) Roduner, E.; Fischer, H. *Chem. Phys.* **1981**, *54*, 261.
(59) Macrae, R. M. *Magn. Reson. Chem.* **2000**, *38*, S33.
(60) Day, P.; Coronado, E. *Chem. Rev.* **2004**, *104*, in press; Dressel, M. *Chem. Rev.* **2004**, *104*, in press; Jerome, D. *Chem. Rev.* **2004**, *104*, in press; Kanoda, K. *Chem. Rev.* **2004**, *104*, in press; Kartsovnik, M. *Chem. Rev.* **2004**, *104*, in press.
(61) Le, L. P.; Luke, G. M.; Sternlieb, B. J.; Wu, W. D.; Uemura, Y. J.; Brewer, J. H.; Riseman, T. M.; Upasani, R. V.; Chiang, L. Y.; Chaikin, P. M. *Europhys. Lett.* **1991**, *15*, 547.
(62) Le, L. P.; Keren, A.; Luke, G. M.; Sternlieb, B. J.; Wu, W. D.; Uemura, Y. J.; Brewer, J. H.; Riseman, T. M.; Upasani, R. V.; Chiang, L. Y.; Kang, W.; Chaikin, P. M.; Csiba, T.; Gruner, G. *Phys. Rev. B* **1993**, *48*, 7284.
(63) Pratt, F. L.; Sasaki, T.; Toyota, N.; Nagamine, K. *Phys. Rev. Lett.* **1995**, *74*, 3892.
(64) Sasaki, T.; Sato, H.; Toyota, N. *Synth. Met.* **1991**, *42*, 2211.
(65) Sasaki, T.; Lebed, A. G.; Fukase, T.; Toyota, N. *Phys. Rev. B* **1996**, *54*, 12969.
(66) Harrison, N.; Biskup, N.; Brooks, J. S.; Balicas, L.; Tokumoto, M. *Phys. Rev. B* **2001**, *63*, 195102.
(67) Dressel, M.; Drichko, N.; Schleuter, J.; Merino, J. *Phys. Rev. Lett.* **2003**, *90*, 167002.
(68) Brandt, E. H. *Phys. Rev. B*, **1988**, *37*, 2349.
(69) Sonier, J. E.; Brewer, J. H.; Kiefl, R. F. *Rev. Mod. Phys.* **2000**, *72*, 769.
(70) Annett, J. F. *Superconductivity, Superfluids, and Condensates*, Oxford University Press: Oxford U.K., 2004.
(71) Sonier, J. E.; Kiefl, R. F.; Brewer, J. H.; Bonn, D. A.; Carolan, J. F.; Chow, K. H.; Dosanjh, P.; Hardy, W. N.; Liang, R.; MacFarlane, W. A.; Mendels, P.; Morris, G. D.; Riseman, T. M.; Schneider, J. W. *Phys. Rev. Lett.* **1994**, *72*, 744.
(72) Yaouanc, A.; Dalmas de Réotier, P.; Brandt, E. H. *Phys. Rev. B* **1997**, *55*, 11107.
(73) Sonier, J. E.; Brewer, J. H.; Kiefl, R. F.; Bonn, D. A.; Dunsiger, S. R.; Hardy, W. N.; Liang, R.; MacFarlane, W. A.; Miller, R. I.; Riseman, T. M.; Noakes, D. R.; Stronach, C. E.; White, M. F., Jr. *Phys. Rev. Lett.* **1997**, *79*, 2875.
(74) Sonier, J. E.; Brewer, J. H.; Kiefl, R. F.; Miller, R. I.; Morris, G. D.; Stronach, C. E.; Gardner, J. S.; Dunsiger, S. R.; Bonn, D. A.; Hardy, W. N.; Liang, R.; Heffner, R. H. *Science* **2001**, *292*, 1692.
(75) Sonier, J. E.; Brewer, J. H.; Kiefl, R. F.; Heffner, R. H.; Poon, K. F.; Stubbs, S. L.; Morris, G. D.; Miller, R. I.; Hardy, W. N.; Liang, R.; Bonn, D. A.; Gardner, J. S.; Stronach, C. E.; Curro, N. J. *Phys. Rev. B* **2002**, *66*, 134501.
(76) Miller, R. I.; Kiefl, R. F.; Brewer, J. H.; Sonier, J. E.; Chakhalian, J.; Dunsiger, S.; Morris, G. D.; Price, A. N.; Bonn, D. A.; Hardy, W. H.; Liang, R. *Phys. Rev. Lett.* **2002**, *88*, 137002.
(77) Blatter, G.; Feigel'man, M. V.; Geshkenbein, V. B.; Larkin, A. I.; Vinokur, V. M. *Rev. Mod. Phys.* **1995**, *66*, 1125.
(78) Clem, J. R. *Phys. Rev. B* **1991**, *43*, 7837.
(79) Lee, S. L.; Zimmermann, P.; Keller, H.; Warden, M.; Savić, I. M.; Schauwecker, R.; Zech, D.; Cubitt, R.; Forgan, E. M.; Kes, P. H.; Li, T. W.; Menovsky, A. A.; Tarnawski, Z. *Phys. Rev. Lett.* **1993**, *71*, 3862.
(80) Lee, S. L.; Pratt, F. L.; Blundell, S. J.; Aegerter, C. M.; Pattenden, P. A.; Chow, K. H.; Forgan, E. M.; Sasaki, T.; Hayes, W.; Keller, H. *Phys. Rev. Lett.* **1997**, *79*, 1563.
(81) Harshman, D. R.; Kleiman, R. N.; Haddon, R. C.; Chichester-hicks, S. V.; Kaplan, M. L.; Rupp, L. W.; Pfiz, T.; Williams, D. L.; Mitzi, D. B. *Phys. Rev. Lett.* **1990**, *64*, 1293.
(82) Le, L. P.; Luke, G. M.; Sternlieb, B. J.; Wu, W. D.; Uemura, Y. J.; Brewer, J. H.; Riseman, T. M.; Stronach, C. E.; Saito, G.; Yamochi, H.; Wang, H. H.; Kini, A. M.; Carlson, K. D.; Williams, J. M. *Phys. Rev. Lett.* **1992**, *68*, 1923.
(83) Harshman, D. R.; Fiory, A. T.; Haddon, R. C.; Kaplan, M. L.; Pfiz, T.; Koster, E.; Shinkoda, I.; Williams, D. L. *Phys. Rev. B* **1994**, *49*, 12990.
(84) Aegerter, C. M.; Hofer, J.; Savic, I. M.; Keller, H.; Lee, S. L.; Ager, C.; Lloyd, S. H.; Forgan, E. M. *Phys. Rev. B* **1998**, *57*, 1253.
(85) Blundell, S. J.; Lee, S. L.; Pratt, F. L.; Aegerter, C. M.; Jestadt, T.; Lovett, B. W.; Ager, C.; Sasaki, T.; Laukhin, V. N.; Laukhina, E.; Forgan, E. M.; Hayes, W. *Synth. Met.* **1999**, *103*, 1925.
(86) Brandt, E. H. *Phys. Rev. Lett.* **1991**, *66*, 3213.
(87) Brandt, E. H. *J. Low Temp. Phys.* **1988**, *73*, 355.
(88) Nishizaki, T.; Sasaki, T.; Fukase, T.; Kobayashi, N. *Phys. Rev. B* **1996**, *54*, R3760.
(89) Blatter, G.; Geshkenbein, V.; Larkin, A.; Nordborg, H. *Phys. Rev. B* **1996**, *54*, 72.
(90) Aegerter, C. M.; Lee, S. L.; Keller, H.; Forgan, E. M.; Lloyd, S. H. *Phys. Rev. B* **1996**, *54*, 15661.
(91) Lee, S. L.; Aegerter, C. M.; Keller, H.; Willemin, M.; StaublePumpin, B.; Forgan, E. M.; Lloyd, S. H.; Blatter, G.; Cubitt, R.; Li, T. W.; Kes, P. *Phys. Rev. B* **1997**, *55*, 5666.
(92) Pratt, F. L.; Lee, S. L.; Aegerter, C. M.; Ager, C.; Lloyd, S. H.; Blundell, S. J.; Ogrin, F. Y.; Forgan, E. M.; Keller, H.; Hayes, W.; Sasaki, T.; Toyota, N.; Endo, S. *Synth. Met.* **2001**, *120*, 1015.
(93) Vinnikov, L. Ya.; Barkov, T. L.; Kartsovnik, M. V.; Kushch, N. D. *Phys. Rev. B* **2000**, *61*, 14358.
(94) Pratt, F. L.; Blundell, S. J.; Husmann, A.; Marshall, I. M.; Lovett, B. W.; Hayes, W.; Lee, S. L.; Ager, C.; Ogrin, F. Y.; Sasaki, T.; Endo, S.; Toyota, N.; Kanoda, K.; Laukhin, V. N.; Laukhina, E.; Watanabe, I.; Nagamine, K. *Physica B* **2000**, *289*, 396.
(95) Charalambous, D.; Kealey, P. G.; Forgan, E. M.; Riseman, T. M.; Long, M. W.; Goupil, C.; Khasanov, R.; Fort, D.; King, P. J. C.; Lee, S. L.; Ogrin, F. *Phys. Rev. B* **2002**, *66*, 054506.
(96) Pratt, F. L.; Marshall, I. M.; Blundell, S. J.; Drew, A.; Lee, S. L.; Ogrin, F. Y.; Toyota, N.; Watanabe, I. *Physica B* **2003**, *326*, 374.
(97) Uemura, Y. J.; Le, L. P.; Luke, G. M.; Sternlieb, B. J.; Wu, W. D.; Brewer, J. H.; Riseman, T. M.; Seaman, C. L.; Maple, M. B.; Ishikawa, M.; Hinks, D. G.; Jorgensen, J. D.; Saito, G.; Yamochi, H. *Phys. Rev. Lett.* **1991**, *66*, 2665.
(98) Uemura, Y. J. *Physica C* **1997**, *282*, 194.
(99) Pratt, F. L.; Blundell, S. J.; Marshall, I. M.; Lancaster, T.; Steer, C. A.; Lee, S. L.; Drew, A.; Divakar, U.; Matsui, H.; Toyota, N. *Polyhedron* **2003**, *22*, 2307.
(100) Pratt, F. L.; Blundell, S. J.; Lancaster, T.; Lee, S.; Toyota, N. *J. Phys. IV* **2004**, *114*, 601.
(101) Penson, K. A.; Kolb, M. *Phys. Rev. B* **1986**, *33*, 1663.
(102) Czart, W. R.; Kobaszkiewicz, S. *Phys. Rev. B* **2001**, *64*, 104511.

(103) Kobayashi, H.; Kobayashi, A.; Cassoux, P. *Chem. Soc. Rev.* **2000**, *29*, 325.
(104) Pratt, F. L.; Lee, S. L.; Blundell, S. J.; Marshall, I. M.; Uozaki, H.; Toyota, N. *Synth. Met.* **2003**, *133*, 489.
(105) Hotta, C.; Fukuyama, H. *J. Phys. Soc. Jpn.* **2000**, *69*, 2577.
(106) McKenzie, R. H. *Comments Condens. Matter Phys.* **1998**, *18*, 309.
(107) Powell, B. J.; McKenzie, R. H. *Phys. Rev. B* **2004**, *69*, 024519.
(108) Kang, W.; Hannahs, S. T.; Chaikin, P. M. *Phys. Rev. Lett.* **1993**, *70*, 3091.
(109) Luke, G. M.; Rovers, M. T.; Fukaya, A.; Gat, I. M.; Larkin, M. I.; Savici, A.; Uemura, Y. J.; Kojima, K. M.; Chaikin, P. M.; Lee, I. J.; Naughton, M. J. *Physica B* **2003**, *326*, 378.
(110) Heffner, R. H.; Smith, J. L.; Willis, J. O.; Birrer, P.; Baines, C.; Gygax, F. N.; Hitti, B.; Lippelt, E.; Ott, H. R.; Schenck, A.; Knetsch, E. A.; Mydosh, J. A.; Maclaughlin, D. E. *Phys. Rev. Lett.* **1990**, *65*, 2816.
(111) Luke, G. M.; Keren, A.; Le, L. P.; Wu, W. D.; Uemura, Y. J.; Bonn, D. A.; Taillefer, L.; Garrett, J. D. *Phys. Rev. Lett.* **1993**, *71*, 1466.
(112) Luke, G. M.; Fudamoto, Y.; Kojima, K. M.; Larkin, M. I.; Merrin, J.; Nachumi, B.; Uemura, Y. J.; Maeno, Y.; Mao, Z. Q.; Mori, Y.; Nakamura, H.; Sigrist, M. *Nature* **1998**, *394*, 558.
(113) Greer, A. J.; Harshman, D. R.; Kossler, W. J.; Goonewardene, A.; Williams, D. L.; Koster, E.; Kang, W.; Kleiman, R. N.; Haddon, R. C. *Physica C* **2003**, *400*, 59.
(114) Rosseinsky, M. J. *J. Mater. Chem.* **1995**, *5*, 1497.
(115) Tanigaki, K.; Prassides, K. *J. Mater. Chem.* **1995**, *5*, 1515.
(116) Uemura, Y. J.; Keren, A.; Le, L. P.; Luke, G. M.; Sternlieb, B. J.; Wu, W. D.; Brewer, J. H.; Whetten, R. L.; Huang, S. M.; Lin, S.; Kaner, R. B.; Diederich, F.; Donovan, S.; Gruner, G.; Holczer, K. *Nature* **1991**, *352*, 605.
(117) Kiefl, R. F.; Macfarlane, W. A.; Chow, K. H.; Dunsiger, S.; Duty, T. L.; Johnston, T. M. S.; Schneider, J. W.; Sonier, J.; Brard, L.; Strongin, R. M.; Fischer, J. E.; Smith, A. B. *Phys. Rev. Lett.* **1993**, *70*, 3987.
(118) Macfarlane, W. A.; Kiefl, R. F.; Dunsiger, S.; Sonier, J. E.; Fischer, J. E. *Phys. Rev. B* **1995**, *52*, R6995.
(119) Uemura, Y. J.; Kojima, K.; Luke, G. M.; Wu, W. D.; Oszlanyi, G.; Chauvet, O.; Forro, L. *Phys. Rev. B* **1995**, *52*, R6991.
(120) Cristofolini, L.; Lappas, A.; Vavekis, K.; Prassides, K.; Derenzi, R.; Ricco, M.; Schenck, A.; Amato, A.; Gygax, F. N.; Kosaka, M.; Tanigaki, K. *J. Phys.: Condens. Matter* **1995**, *7*, L567.
(121) Brouet, V.; Alloul, H.; Yoshinari, Y.; Forro, L. *Phys. Rev. Lett.* **1996**, *76*, 3638.
(122) Simovic, B.; Jerome, D.; Rachdi, F.; Baumgartner, G.; Forro, L. *Phys. Rev. Lett.* **1999**, *82*, 2298.
(123) Janossy, A.; Nemes, N.; Feher, T.; Oszlanyi, G.; Baumgartner, G.; Forro, L. *Phys. Rev. Lett.* **1997**, *79*, 2718.
(124) Pratt, F. L.; Blundell, S. J.; Jestädt, T.; Lovett, B. W.; Husmann, A.; Marshall, I. M.; Hayes, W.; Monkman, A.; Watanabe, I.; Nagamine, K.; Martin, R.; Holmes, A. B. *Physica B* **2000**, *289*, 625.
(125) Jestädt, Th. Thesis, University of Oxford, 1999.
(126) Pratt, F. L.; Blundell, S. J.; Marshall, I. M.; Lancaster, T.; Husmann, A.; Steer, C.; Hayes, W.; Fischmeister, C.; Martin, R. E.; Holmes, A. B. *Physica B* **2003**, *326*, 34.
(127) Su, W. P.; Schrieffer, J. R.; Heeger, A. J. *Phys. Rev. B* **1980**, *22*, 2099.
(128) Heeger, A. J.; Kivelson, S.; Schrieffer, J. R.; Su, W. P. *Rev. Mod. Phys.* **1988**, *60*, 781.
(129) Fisher, A. J.; Hayes, W.; Wallace, D. S. *J. Phys.: Condens. Matter* **1989**, *1*, 5567.
(130) Nagamine, K.; Ishida, K.; Matsuzaki, T.; Nishiyama, K.; Kuno, Y.; Yamazaki, T. *Phys. Rev. Lett.* **1984**, *53*, 1763.
(131) Pratt, F. L.; Hayes, W.; Mitchell, G. R.; Rossi, B.; Kiani, M. S.; Malhotra, B. D.; Pandey, S. S.; Milton, A.; Monkman, A. P. *Synth. Met.* **1993**, *55*, 677.
(132) Hayes, W. *Philos. Trans. R. Soc. London, Ser. A* **1995**, *350*, 249.
(133) Nishiyama, K.; Ishida, K.; Nagamine, K.; Matsuzaki, T.; Kuno, Y.; Shirakawa, H.; Kiefl, R.; Brewer, J. H. *Hyperfine Interact.* **1986**, *32*, 551.
(134) Fisher, A. J.; Hayes, W.; Pratt, F. L. *J. Phys.: Condens. Matter* **1991**, *3*, 9823.
(135) Jestädt, Th.; Sivia, D. S.; Cox, S. F. J. *Hyperfine Interact.* **1997**, *106*, 45.
(136) Pratt, F. L.; Valladares, R. M.; Pattenden, P. A.; Blundell, S. J.; Hayes, W.; Fisher, A. J.; Monkman, A. P.; Malhotra, B. D.; Nagamine, K. *Synth. Met.* **1995**, *69*, 231.
(137) Pratt, F. L.; Ishida, K.; Nagamine, K.; Pattenden, P. A.; Jestädt, T.; Chow, K. H.; Blundell, S. J.; Hayes, W.; Monkman, A. P. *Synth. Met.* **1997**, *84*, 943.
(138) Pratt, F. L.; Blundell, S. J.; Pattenden, P. A.; Hayes, W.; Chow, K. H.; Monkman, A. P.; Ishiguro, T.; Ishida, K.; Nagamine K. *Hyperfine Interact.* **1997**, *106*, 33.
(139) Mizoguchi, K.; Kume, K. *Solid State Commun.* **1994**, *89*, 971.
(140) Pratt, F. L. *J. Phys.: Condens. Matter* **2004**, in press.
(141) Mizoguchi, K. *Jpn. J. Appl. Phys.* **1995**, *34*, 1.
(142) Mizoguchi, K. *Synth. Met.* **2001**, *199*, 35.
(143) Pratt, F. L.; Blundell, S. J.; Hayes, W.; Ishida, K.; Nagamine, K.; Monkman, A. P. *Phys. Rev. Lett.* **1997**, *79*, 2855.
(144) Risch, R.; Kehr, K. W. *Phys. Rev. B* **1992**, *46*, 5246.
(145) Bourdeaux, D. S.; Chance, R. R.; Bredas, J. L.; Silbey, R. *Phys. Rev. B* **1983**, *28*, 6297.
(146) Blundell, S. J.; Pratt, F. L.; Marshall, I. M.; Steer, C. A.; Hayes, W.; Husmann, A.; Fischmeister, C.; Martin, R. E.; Holmes, A. B. *J. Phys.: Condens. Matter* **2002**, *14*, 9987.
(147) Jeyadev, S.; Conwell, E. M. *Phys. Rev. B* **1987**, *35*, 6523.
(148) Maki, K. *Phys. Rev. B* **1982**, *26*, 2181.
(149) Valladares, R. M.; Hayes, W.; Fisher, A. J.; Stoneham, A. M. *J. Phys.: Condens. Matter* **1993**, *5*, 7049; Pratt, F. L.; Blundell, S. J. Unpublished.
(150) Nagamine, K. *Eur. J. Phys.* **2002**, *13*, 189.
(151) Morenzoni, E.; Kottmann, F.; Maden, D.; Matthias, B.; Meyberg, M.; Prokscha, T.; Wutzke, T.; Zimmermann, U. *Phys. Rev. Lett.* **1994**, *72*, 2793.
(152) Harshman, D. R.; Mills, A. P.; Beveridge, J. L.; Kendall, K. R.; Morris, G. D.; Senba, M.; Warren, J. B.; Rupaal, A. S.; Turner, J. H. *Phys. Rev. B* **1987**, *36*, 8850.
(153) Nagamine, K.; Miyake, Y.; Shimomura, K.; Birrer, P.; Iwasaki, M.; Strasser, P.; Kuga, T. *Phys. Rev. Lett.* **1995**, *74*, 4811.
(154) Jackson, T. J.; Binns, C.; Forgan, E. M.; Morenzoni, E.; Niedermayer, C.; Gluckler, H.; Hofer, A.; Luetkens, H.; Prokscha, T.; Riseman, T. M.; Schatz, A.; Birke, M.; Litterst, J.; Schatz, G.; Weber, H. P. *J. Phys.: Condens. Matter* **2000**, *12*, 1399.
(155) Luetkens, H.; Korecki, J.; Morenzoni, E.; Prokscha, T.; Birke, M.; Gluckler, H.; Khasanov, R.; Klauss, H. H.; Slezak, T.; Suter, A.; Forgan, E. M.; Niedermayer, C.; Litterst, F. J. *Phys. Rev. Lett.* **2003**, *91*, 017204.
(156) Jackson, T. J.; Riseman, T. M.; Forgan, E. M.; Gluckler, H.; Prokscha, T.; Morenzoni, E.; Pleines, M.; Niedermayer, C.; Schatz, G.; Luetkens, H.; Litterst, J. *Phys. Rev. Lett.* **2000**, *84*, 4958.
(157) Niedermayer, C.; Forgan, E. M.; Gluckler, H.; Hofer, A.; Morenzoni, E.; Pleines, M.; Prokscha, T.; Riseman, T. M.; Birke, M.; Jackson, T. J.; Litterst, J.; Long, M. W.; Luetkens, H.; Schatz, A.; Schatz, G. *Phys. Rev. Lett.* **1999**, *83*, 3932.
(158) Suter, A.; Morenzoni, E.; Khasanov, R.; Luetkens, H.; Prokscha, T.; Garifianov, N. *Phys. Rev. Lett.* **2004**, *92*, 087001.

CR030632E